

ON THE USE OF INNOVATIVE TECHNIQUES TO  
EVALUATE THE HEALTH OF STRUCTURAL  
SYSTEMS

A Dissertation

Presented to the Faculty of the Graduate School  
of Cornell University

in Partial Fulfillment of the Requirements for the Degree of  
Doctor of Philosophy

by

Christopher Jason Stull

May 2010

© 2010 Christopher Jason Stull

ALL RIGHTS RESERVED

# ON THE USE OF INNOVATIVE TECHNIQUES TO EVALUATE THE HEALTH OF STRUCTURAL SYSTEMS

Christopher Jason Stull, Ph.D.

Cornell University 2010

The present document reports on three separate research efforts which aim to marry, in novel ways, existing techniques from experimental and computational mechanics, inverse problems, and Bayesian statistical inference, in order to assess the condition of structural systems.

The first chapter offers a quantitative and objective means for assessing the reserve capacity in bridges damaged by over-height truck strikes. Terrestrial laser scanning systems are employed to record the damaged geometry of the bridge and image-processing techniques are used to create corresponding solid models. These solid models are then integrated into finite element models of the damaged bridge, which are analyzed in order to quantify the effects of the damage. Results are promising within the context of accurately characterizing the damaged geometry, but it was found that further development of the former two technologies would be required before this could be considered a viable bridge assessment technique.

The second chapter offers a means of inferring initial, “denting” imperfection fields within cylindrical shell structures, employing sparse displacement measurements observed at service-loading conditions. The inverse problem posed by the adoption of a model-updating scheme is solved using a genetic algorithm. This genetic algorithm is extended to include a divide-and-conquer approach which subdivides the problem, effectively providing an incremental

solution. Results are promising in that target imperfections are reliably inferred from simulated experimental data. These imperfection fields are then employed to make reasonably accurate predictions of the ultimate strengths of the imperfect shell structures.

The final chapter offers an outline of a health monitoring scheme for application to naval hull structural systems. A model-updating scheme is adopted and the resulting inverse problem is solved using: a functional optimization approach (employing a genetic algorithm) and a Bayesian statistical inference approach (employing a sequential Monte Carlo algorithm). As a proof-of-concept, two distinct problems are proposed and solved: detecting corrosion within the side-shells of a hull and detecting internal blast damage, affecting the internal framing of a hull. Reliable predictions of both damage scenarios are made using each approach, with the Bayesian approach providing quantification of uncertainty within these predictions.

## BIOGRAPHICAL SKETCH

Christopher Stull was born on November 12, 1980 in the town of Vincennes, Indiana, to parents David and Debra Stull. He began his academic career at St. John Lutheran School, after which time he was enrolled in Rivet Middle / High School where he graduated in 1999, sharing the honor of salutatorian with a fellow classmate. The following semester, Christopher entered the engineering program at Purdue University in West Lafayette, Indiana, and subsequently chose to major in civil engineering. In addition to his coursework, Christopher participated in various co-ops / internships, and in the Fall of 2004, he earned a bachelor's degree, with distinction. Christopher then moved, with his wife (of negative two months), Caroline, to Pittsburgh, Pennsylvania to pursue a master's degree at the University of Pittsburgh, working with Dr. Christopher Earls. In the Summer of 2006, after earning this degree, Christopher and Caroline moved to Ithaca, New York, where Christopher enrolled in Cornell University to continue working with Dr. Earls, in pursuit of a doctoral degree.

For my wife.

## ACKNOWLEDGEMENTS

To my wife, Caroline: Thank you for your undying support during my (our) pursuit of both my doctoral and master's degrees. I don't think either of us expected that we would celebrate our fifth wedding anniversary before I finished.

To Mom and Dad: Thank you both for always encouraging me to work hard and keep my head up throughout my nearly 25 year long academic career. I'm out of degrees now.

To Dr. Earls: Words cannot express the gratitude I have for the support and wisdom I have received as your advisee. I am both honored and proud to have worked with you during my graduate career.

To my doctoral committee members, Dr. Phaedon-Stelios (*a.k.a.* "Steve") Koutsourelakis and Dr. Charles Van Loan: Thank you very much for your time and your effort expended on my behalf.

I would also like to acknowledge the agencies from whom I received funding to pursue both my doctoral and master's degrees: the Pennsylvania Department of Transportation and the Office of Naval Research. Also, a special thanks to Dr. Paul Hess for his guidance during the latter two-thirds of my graduate career.

Finally, I would be remiss if I did not also thank my brother, Nicholas Stull, as well as Emily Leigh, Tom Howell, and John Brigham for their friendship and support throughout my graduate career.

## TABLE OF CONTENTS

Biographical Sketch . . . . .	iii
Dedication . . . . .	iv
Acknowledgements . . . . .	v
Table of Contents . . . . .	vi
List of Figures . . . . .	viii
List of Tables . . . . .	x
<b>1 A rapid assessment methodology for bridges damaged by truck strikes</b>	<b>1</b>
1.1 Introduction . . . . .	1
1.2 Description of bridge assessment methodology . . . . .	3
1.2.1 Terrestrial laser scanning . . . . .	4
1.2.2 Image processing . . . . .	9
1.2.3 Computational mechanics . . . . .	12
1.3 Field test results . . . . .	13
1.3.1 Description of subject bridge . . . . .	13
1.3.2 Description of finite element model . . . . .	16
1.3.3 Results and discussion . . . . .	17
1.4 Conclusions . . . . .	22
<b>2 A posteriori initial imperfection identification in shell buckling problems</b>	<b>24</b>
2.1 Introduction . . . . .	24
2.1.1 Background . . . . .	25
2.1.2 Paper organization . . . . .	29
2.2 Problem formulation . . . . .	29
2.2.1 Forward problem . . . . .	29
2.2.2 Inverse problem . . . . .	33
2.3 Model problem . . . . .	35
2.3.1 Forward modeling . . . . .	38
2.3.2 Inverse solution . . . . .	39
2.4 Results and discussion . . . . .	47
2.5 Conclusions . . . . .	52
<b>3 Model-based structural health monitoring of naval ship hulls</b>	<b>54</b>
3.1 Introduction . . . . .	54
3.1.1 Background . . . . .	56
3.1.2 Paper organization . . . . .	59
3.2 Formulation . . . . .	60
3.2.1 Forward problem . . . . .	61
3.2.2 Inverse problem . . . . .	62
3.2.3 Parameterization of damage . . . . .	66
3.3 Example problems . . . . .	72

3.3.1	Example Problem 1 . . . . .	73
3.3.2	Example Problem 2 . . . . .	75
3.3.3	Stochastic search approaches . . . . .	76
3.4	Results and Discussion . . . . .	84
3.4.1	Example Problem 1 . . . . .	86
3.4.2	Example Problem 2 . . . . .	90
3.5	Conclusions . . . . .	95
	<b>Bibliography</b>	<b>97</b>

## LIST OF FIGURES

1.1	Example of catastrophic bridge damage due to a vehicular impact.	2
1.2	Schematic of time-of-flight TLS system metrology. . . . .	6
1.3	Schematic of continuous wave TLS system metrology. . . . .	6
1.4	Schematic of TLS system at a small stand-off distance. . . . .	8
1.5	Example of point cloud data registration of a region of the subject bridge. . . . .	10
1.6	Example of “wrapped” surface created in Geomagic. . . . .	11
1.7	Example of boundaries around tessellated surface created in Geomagic. . . . .	12
1.8	Structural steel framing plan for subject bridge. . . . .	14
1.9	Example of point cloud from damaged region of subject bridge. .	16
1.10	(a) End span; and (b) Three span uniform deck pressure load configurations. . . . .	18
1.11	$\lambda$ -displacement plot of midspan of Span 1 for end span load configuration. . . . .	19
1.12	$\lambda$ -displacement plot of midspan of Span 2 for end span load configuration. . . . .	20
1.13	Percent difference in top-of-steel deformation between damaged and undamaged models for end span load configuration. .	20
1.14	$\lambda$ -displacement plot of midspan of Span 1 for three span load configuration. . . . .	21
1.15	$\lambda$ -displacement plot of midspan of Span 2 for three span load configuration. . . . .	21
1.16	Percent difference in top-of-steel deformation between damaged and undamaged models for three span load configuration. .	22
1.17	Initial and final deformed configurations of the web for three-span load configuration (not to scale). . . . .	22
2.1	Configurations for forward and inverse problems. . . . .	30
2.2	Edge loaded barrel vault shell example structure. . . . .	36
2.3	Representative dent imperfection (magnified 1000 $\times$ ). . . . .	37
2.4	Summary of mesh convergence study results. . . . .	38
2.5	Truncated Gaussian PDF used to mutate RBF centers away from vertices. . . . .	43
2.6	Schematic depiction of stochastic search approach. . . . .	44
2.7	Actual initial configurations with associated RBF parameters: single dent on left; double dent on right. . . . .	47
2.8	Representative single dent solutions using one (left) and four (center) RBFs in inverse solution; actual imperfection on right. .	48
2.9	Representative double dent solution using four RBFs in inverse solution: approximate imperfection on left; actual imperfection on right. . . . .	50

3.1	Transformation of hull side shells into a two-dimensional representation . . . . .	68
3.2	Gross dimensions of idealized ship structural system . . . . .	73
3.3	Schematic of finite element mesh for Example Problem 1 displaying data sampling configuration (white triangles) . . . . .	74
3.4	Schematic of finite element mesh for Example Problem 2 displaying data sampling configuration (white triangles) . . . . .	76
3.5	Features of the genetic algorithm employed for the paper . . . . .	78
3.6	Schematic of parents undergoing single-point crossover; the dashed line represents the <i>random</i> point at which parameters are swapped . . . . .	79
3.7	Schematic of divide-and-conquer solution scheme . . . . .	81
3.8	Example Problem 1 - Test Case A (a) target damage configuration; (b) representative solution from the GA; (c) maximum likelihood solution from the SMC (gray lines indicate locations of transverse bulkheads) . . . . .	87
3.9	Example Problem 1, Test Case A - Posterior mean and posterior quantiles of thickness variation along lines at (a) $\hat{i} - Coord. = 3270$ and (b) $\hat{j} - Coord. = -260$ obtained using the Bayesian inference scheme described in Section 3.3.3 . . . . .	88
3.10	Example Problem 1, Test Case A - Posterior density of error standard deviation $\sigma_e$ (Equation (3.13)) compared with the reference value $\sigma_{e,ref} = 0.033$ used in generating the data $\mathbf{U}_{obs}$ . . . . .	89
3.11	Example Problem 1 - Test Case B (a) target damage configuration; (b) representative solution from the GA; (c) maximum likelihood solution from the SMC (gray lines indicate locations of transverse bulkheads) . . . . .	90
3.12	Example Problem 1, Test Case B - Posterior mean and posterior quantiles of thickness variation along lines at (a) $\hat{i} - Coord. = 2095$ and (b) $\hat{j} - Coord. = 260$ obtained using the Bayesian inference scheme described in Section 3.3.3 . . . . .	91
3.13	Example Problem 1, Test Case B - Posterior density of error standard deviation $\sigma_e$ (Equation (3.13)) compared with the reference value $\sigma_{e,ref} = 0.033$ used in generating the data $\mathbf{U}_{obs}$ . . . . .	92
3.14	Example Problem 2 - Test Case A (a) target damage configuration; (b) representative solution from the GA; (c) maximum likelihood solution from the SMC (gray lines indicate locations of transverse bulkheads) . . . . .	94
3.15	Example Problem 2 - Test Case B (a) target damage configuration; (b) representative solution from the GA; (c) maximum likelihood solution from the SMC (gray lines indicate locations of transverse bulkheads) . . . . .	95

## LIST OF TABLES

2.1	Comparison of results for representations of single dent with one RBF . . . . .	48
2.2	Comparison of results for representations of single dent with four RBFs . . . . .	49
2.3	Comparison of results for representations of double dent with four RBFs . . . . .	50
2.4	Comparison of single dent buckling results $(LPF_{cr})_{obs} = 1.869$ . .	52
2.5	Comparison of double dent buckling results $(LPF_{cr})_{obs} = 1.875$ .	52
3.1	Data from active duty naval warships [18] . . . . .	55
3.2	Summary of the divide-and-conquer GA employed . . . . .	82
3.3	Basic steps of the <i>Adaptive</i> SMC algorithm employed . . . . .	85
3.4	Test cases examined for Example Problem 1 . . . . .	86
3.5	Comparison metric values (Equation (3.20)) for Example Problem 1. In the SMC columns the average $\pm$ st. deviation values are provided which were estimated from the particles approximating the posterior. . . . .	90
3.6	Test cases examined for Example Problem 2 . . . . .	93
3.7	Comparison metric values (Equation (3.20)) for Example Problem 2. In the SMC columns the average $\pm$ st. deviation values are provided which were estimated from the particles approximating the posterior. . . . .	95

CHAPTER 1  
A RAPID ASSESSMENT METHODOLOGY FOR BRIDGES DAMAGED  
BY TRUCK STRIKES<sup>1</sup>

**Abstract**

The present research aims to develop a methodology to rapidly assess bridges with damage to the superstructure, caused by overheight trucks or lower-than-average overhead clearance. Terrestrial laser scanning and image processing techniques are combined with the finite element method to arrive at an analytical model which is more accurate, with respect to the complex geometrical aspects of the bridge in its damaged configuration. “Virtual load testing” may subsequently be carried out on this analytical model to determine the reserve capacity of the structure in an objective manner.

**1.1 Introduction**

The Federal Highway Administration reports that approximately forty-two percent of the bridges in the United States are of the type “Stringer / Multi-Beam or Girder,” [1] with many of these being highway under- or overpasses. Unfortunately, it is not uncommon for these structures to undergo damage due to vehicular impacts arising from scenarios such as: (1) an over-height vehicle encountering a bridge with a particularly low overhead clearance; (2) a vehicle encountering a bridge for which the overhead clearance is non-conservatively

---

<sup>1</sup>C.J. STULL AND C.J. EARLS. A RAPID ASSESSMENT METHODOLOGY FOR BRIDGES DAMAGE BY TRUCK STRIKES. *STEEL AND COMPOSITE STRUCTURES*, 9(3):223-37, 2009.

mis-labeled, as a result of re-surfacing of the underlying roadway; or (3) an out-of-control vehicle impacting a bridge pier / abutment [33]. Indeed, it was found in the State of Maryland alone that there was an eighty-one percent increase in collisions arising from scenarios (1) or (2) from the period of 1995–2000 [40]; this study also shows that sixty-two percent of states consider this to be a significant concern.

With respect to scenarios (1) and (2) above, the ensuing damage to the underside of the bridge may be catastrophic in nature (Figure 1.1). However, it is more common that the bridge will sustain minor to moderate damage, while remaining intact. While such damage varies dramatically, depending upon the nature of the impact, there are common characteristics accompanying these vehicular impacts. These may include: (1) inelastic deformation and / or rupture of the longitudinal steel girders; (2) buckling of the transverse members; and / or (3) a reduction and / or loss of the composite action at the steel girder / concrete deck interface.



Figure 1.1: Example of catastrophic bridge damage due to a vehicular impact.

Design office procedures used to evaluate the reserve capacity of such post-

event structures typically rely heavily on “engineering judgment” and greatly simplified calculations. As a result, quantitative objectivity is difficult to ensure. The present research offers a more quantitative and arguably more objective means for assessing the reserve capacity in damaged bridges.

The present discussion is organized as follows: Section 1.2 furnishes an overview and discussion of the techniques used to support the bridge assessment methodology introduced in this research; Section 1.3 describes a field deployment of the proposed methodology; and Section 1.4 provides conclusions that may be drawn from the present research.

## **1.2 Description of bridge assessment methodology**

The proposed bridge assessment methodology employs three primary technologies: (1) terrestrial laser scanning (TLS), (2) image processing, and (3) computational mechanics, by way of finite element analysis (FEA). The goal of the present research is not to develop or improve upon these existing technologies, but rather to link them in order to provide a novel approach for assessing bridges with damage due to vehicular impacts. A brief background of the former two technologies, as well as their relation to the present research, follows. The commercially available, nonlinear FEA software package, ADINA Version 8.4.1 [56], is employed in the present research; however, the techniques described are general, in that a similarly capable FEA software package may be implemented as an alternative to ADINA.

### **1.2.1 Terrestrial laser scanning**

Terrestrial laser scanning (TLS) describes an automated process that has been successfully employed within the context of historical preservation and architectural study. TLS systems have also been employed in the civil engineering community for a number of years, primarily playing a supporting role in various surveying tasks typical to construction sites. Improved computational technologies and data management strategies, however, have expanded the applicability of TLS systems to additional fields. Goedert *et al.* proposed a technique that employed a TLS system and rapid prototyping technologies to significantly increase the efficiency of developing construction models for architectural firms [45]. Fuchs *et al.* employed a TLS system as a tool for the nondestructive evaluation of various highway bridge components [41, 42]. Su *et al.* implemented a TLS system as a tool to monitor excavation progress on construction sites, as well as ground movements associated with these excavations for use in geotechnical analyses [94].

#### **Role in bridge assessment methodology**

Within the context of the present research, TLS is the process of obtaining point cloud data containing the precise location of points on an object as follows: (1) a TLS system emits laser radiation, in the form of a beam, directed toward an object (or a portion of an object) of interest; (2) the laser radiation is scattered and some returns to the TLS system; and (3) an onboard computer calculates the object's standoff distance based upon data related to this reflected laser radiation. The standoff distance, together with an angular position, is then mapped onto a three-dimensional coordinate system. The process is repeated throughout the

field-of-view of the TLS system at a particular instrument location, resulting in a three-dimensional point cloud data set of the object (or a portion of the object). If only a portion of the object is captured, multiple TLS system set-ups are required; for each instrument location, a local, instrument-centered coordinate system is inherited by each resulting point cloud data set.

Several different TLS system technologies are commercially available for applications such as those mentioned above. For the present research, the authors considered two of these: time-of-flight and continuous wave, or phase-based systems. The primary differences between these two TLS systems lie in how the beam is emitted from the laser diode, and the method of treating the return signal. In a time-of-flight system, the laser diode emits a pulsed beam, that is subsequently scattered by the target surface, and partially reflected back to the TLS system. The difference in time between emission and reception of this pulse is then used to compute the standoff distance between the instrument location and the target surface (Figure 1.2). The continuous wave system, as the name implies, operates with a continuously emitted beam. Determination of the standoff distance is subsequently obtained by measuring the phase-shift between the emitted and received waves (Figure 1.3). It is noted that the TLS systems employed for the present research are the CYRAX 2500 time-of-flight system, manufactured by Cyra Technologies Inc., and the Zoller + Fröhlich (Z+F) Imager 5003 continuous wave system.

A comparison of these two TLS systems revealed that the data acquisition time required by the Z+F system is approximately one-half that of CYRAX system. To put this into context, the time required by the latter system to obtain raw point cloud data of the subject bridge chosen for the present research (de-

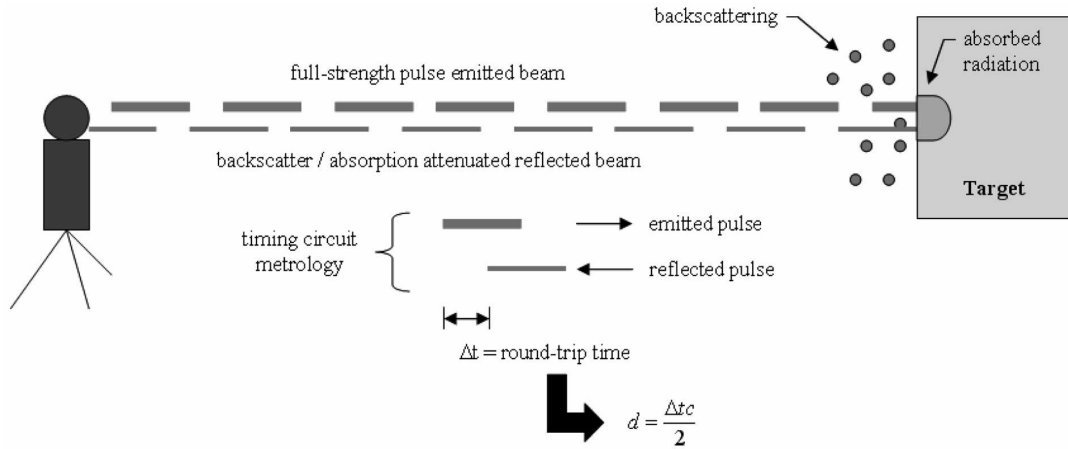


Figure 1.2: Schematic of time-of-flight TLS system metrology.

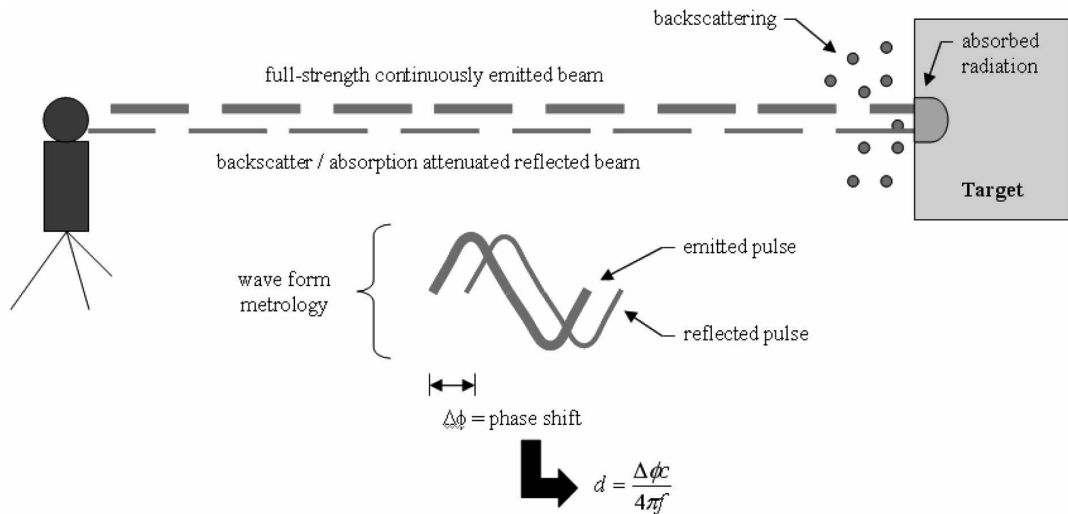


Figure 1.3: Schematic of continuous wave TLS system metrology.

scribed in the sequel) is between 8 and 12 hours. However, despite the savings in data acquisition time exhibited by the Z+F system, the point cloud data was observed to be of insufficient accuracy to develop the parasolid model required for the bridge assessment methodology subsequently described. Thus, all work presented herein is based upon point cloud data obtained via the CYRAX 2500 time-of-flight system. The previously mentioned time requirement of 8 to 12 hours is significantly reduced when point cloud data of only a portion of the

bridge is required; justification for this reduced requirement will be provided in the sequel.

### **Practical considerations**

Lichti *et al.* provides a thorough discussion of the various intrinsic errors associated with TLS systems [65]; for the purposes of this paper, such intrinsic errors are characterized as “noise,” and will be addressed subsequently. However, two operational characteristics of TLS systems are of particular importance with respect to the research reported upon herein, both of which stem from the occlusion of certain data.

First, it is important to note the nature of the acquired data as it relates to the adopted finite element modeling strategy. In the present research, shell finite elements are employed to represent the longitudinal steel girders; these shells are defined along the mid-plane of the constituent cross-sectional plate components. Therefore, data obtained about the shape of an object, as a volume, must then be reinterpreted to represent the shape of the object’s middle surface. While this does not pose a problem for planar surfaces, in which a simple offset of the scanned surface is required, a non-planar surface, such as that encountered when dealing with significantly damaged super-structural elements, can provide some difficulty when making the transition between raw point cloud data and a parasolid model suitable for use with finite element software.

A second problematic characteristic emanates from obstructions that prevent the laser beam from reaching a structural member of interest, thus resulting in an incomplete point cloud data set, with respect to the entire bridge. The

compact spacing of girders characteristic to highway under- and overpasses often results in such a situation in which one or more girders, located in the background, with respect to the orientation of the TLS system, are occluded from view by those in the foreground. Additionally, lateral bracing as well as any non-structural components (e.g. storm drainage pipes) will also result in an occlusion of data.

While a plausible solution to the above is to institute multiple TLS system set-ups, in which data are obtained at smaller stand-off distances from the girder(s) of interest, such a solution violates the imperative of proposing a rapid bridge assessment methodology (i.e. the time requirements and computational demand imposed by additional scans and subsequent image processing increase significantly). Two additional issues are also encountered as stand-off distances are decreased: (1) the angle of incidence with respect to the web increases, resulting in poor accuracy of the associated point cloud data [65]; and (2) the bottom flange of the girder becomes a new obstruction for the bottom of the web (Figure 1.4).

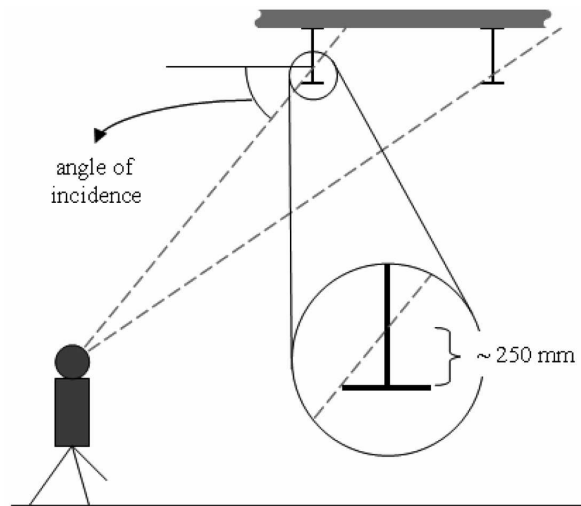


Figure 1.4: Schematic of TLS system at a small stand-off distance.

Taking into account the above issues, it is recommended that point cloud data from only the damaged girder(s), versus the entire bridge, are required for this bridge assessment methodology; the ensuing parasolid models would then replace the corresponding portions within a preexisting, as-built, finite element model of the same bridge. While this may still require point cloud data from interior girders, damage scenarios to which this bridge assessment methodology apply are typically localized to the fascia girder, a location for which data has exhibited a reasonably high level of accuracy. This decision also supports the research imperative of proposing a rapid bridge assessment methodology, in that girders that do not exhibit damage do not need to be scanned.

### **1.2.2 Image processing**

In this work, image processing consists of all the steps necessary to arrive at the required parasolid model for implementation into ADINA. This may be broken up into the following two steps: (1) registration of the point cloud data sets; and (2) approximation of the damaged region by way of a parasolid model, based upon a point cloud “template.”

Point cloud registration is the process of merging multiple point clouds (each in local, instrument-centered coordinate systems), emanating from the requisite TLS system set-ups, into a point cloud data set that represents the entire assembly (within a single, global reference frame). While all point cloud registration for the present research is achieved by way of the registration tools in Geomagic Studio 9 [58], the basic steps present in most registration algorithms are as follows: (1) choose a reference point cloud, to which an unregistered point cloud(s)

will be registered; (2) detect / match coincident features of the reference / unregistered point clouds (e.g. bolts); and (3) rotate / translate the unregistered point cloud(s) to align with the reference point cloud. These steps may be manual and / or automatic (e.g. Geomagic allows the choice of reference / unregistered point clouds and targets), but fine-tuning of the resulting point cloud is performed automatically. As an example, consider Figure 1.5, in which three point cloud data sets of a region of a subject bridge are registered; to result in a single point cloud data set of this region.

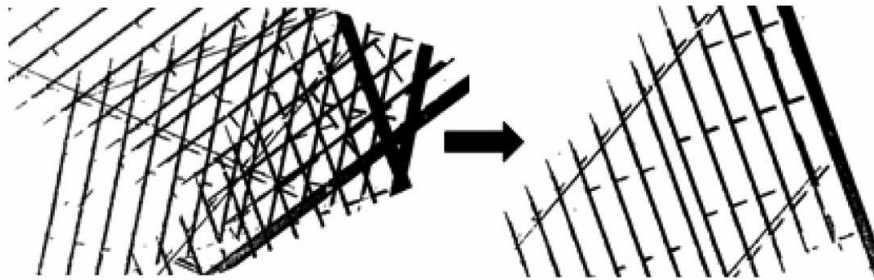


Figure 1.5: Example of point cloud data registration of a region of the subject bridge.

Additional functions in Geomagic allow this newly registered point cloud to be “wrapped” by a surface consisting of triangular polygons. This wrapping function is essentially a best-fit tessellation of the point cloud representing the surface, and also accounts for the inherent “noise” mentioned previously. The labeling of this surface as a point cloud “template,” comes from the following: as seen in the upper left corner of Figure 1.6, the cross-section of point cloud data only represents the exterior face of the girder, and the resulting wrapped surface approximates this exterior face. Furthermore, incomplete point cloud data results in gaps in the wrapped surface (Figure 1.6), and such gaps in surface data may not exist in the completed parasolid model; these gaps as they cause failure within the automated routines typically employed by finite ele-

ment software systems. Therefore, while the wrapped surface may not serve as the parasolid model, it may serve as a template for construction of this parasolid model.

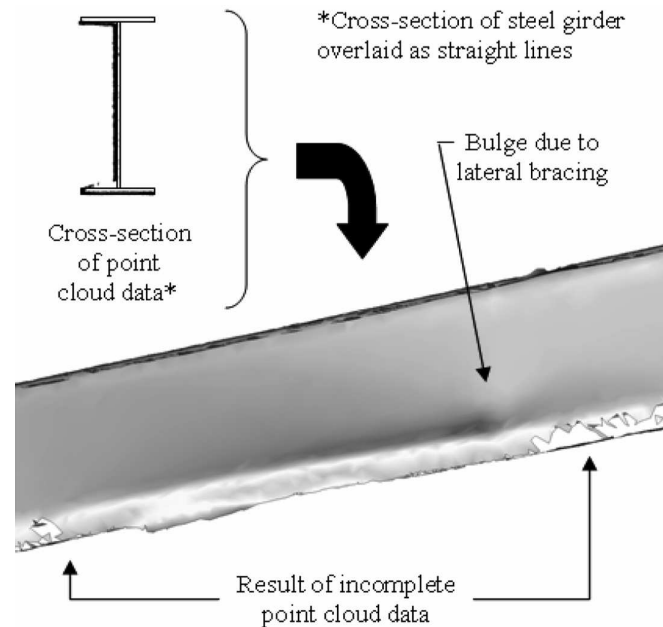


Figure 1.6: Example of “wrapped” surface created in Geomagic.

The parasolid model is then derived from this template using a two-part process: borders of the constituent cross-sectional plate components are drawn in AutoCAD 2006 [57] and the shapes that represent these plate components are then filled-in in SolidWorks Office 2007 [19]; an example of the bordering is given in Figure 1.7. It is pointed out that this process can likely be performed entirely within SolidWorks; however, in the interest of expediency AutoCAD is also employed. It is also pointed out that ADINA permits the importation of solid geometry within the parasolid format; neither Geomagic nor AutoCAD currently have the capability to output to this file format, but SolidWorks does.

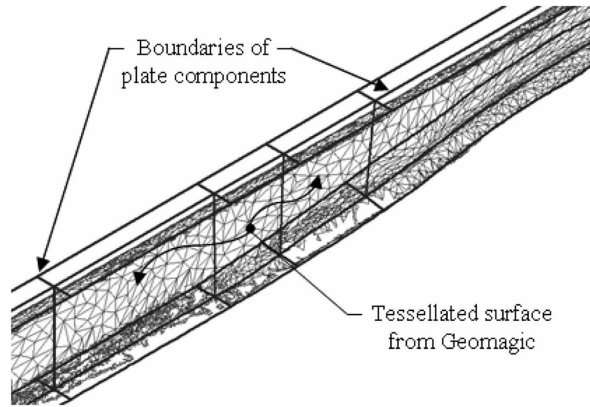


Figure 1.7: Example of boundaries around tessellated surface created in Geomagic.

### 1.2.3 Computational mechanics

The purpose of the computational mechanics portion of the bridge assessment methodology is to provide insight in to the extent to which the complex damaged geometry affects the behavioral characteristics of the structure, as compared with the undamaged structure. Therefore, only practical considerations for the modeling of such damaged regions are discussed herein. One obvious concern is with regard to maintaining geometric continuity at locations where the damaged parasolid model is inserted. As previously discussed, only a small portion of the structure is being modeled by way of point cloud data; thus, it is crucial that this damaged section fit within the undamaged finite element model, seamlessly. For the present research, this continuity is achieved by including a portion of the undamaged section of the fascia girder on each end of the inserted parasolid model. If the dimensions employed in generating the parasolid model in SolidWorks are identical to those considered in generating the finite element model in ADINA, there is no difference in the resulting finite element mesh.

The strength of the described methodology is the ability to relatively quickly map the complex post-event structural geometry and subsequently construct a nonlinear finite element model for use in “virtual load testing.” The method outlined in the foregoing does not explicitly account for changes in material response, fracture, changes in composite action, or the presence of residual stresses. These effects can be considered in the subsequent finite element models, but such inclusion will necessarily be less objective than the model geometry. Compared with current techniques, these shortcomings of the present methodology may not be critical.

### **1.3 Field test results**

As a means for demonstrating the application of the previously described techniques, a damaged slab-on-steel I-girder bridge is considered.

#### **1.3.1 Description of subject bridge**

##### **Structural configuration**

The subject bridge consists of a three-span continuous steel I-girder superstructure with a 30° longitudinally configured skew angle oriented from northwest to southeast (Figure 1.8); it is noted that interior piers are parallel to this skew angle as well. The primary components of the superstructure are W610×113 steel I-girders, with top flanges embedded in a 190 mm concrete deck. As a result of this embedment, it is assumed that the steel girders and

deck enjoy full composite action. The lengths of the three spans are 8230 mm, 15240 mm, and 8230 mm, respectively (these are designated as Span 1, Span 2, and Span 3, respectively).

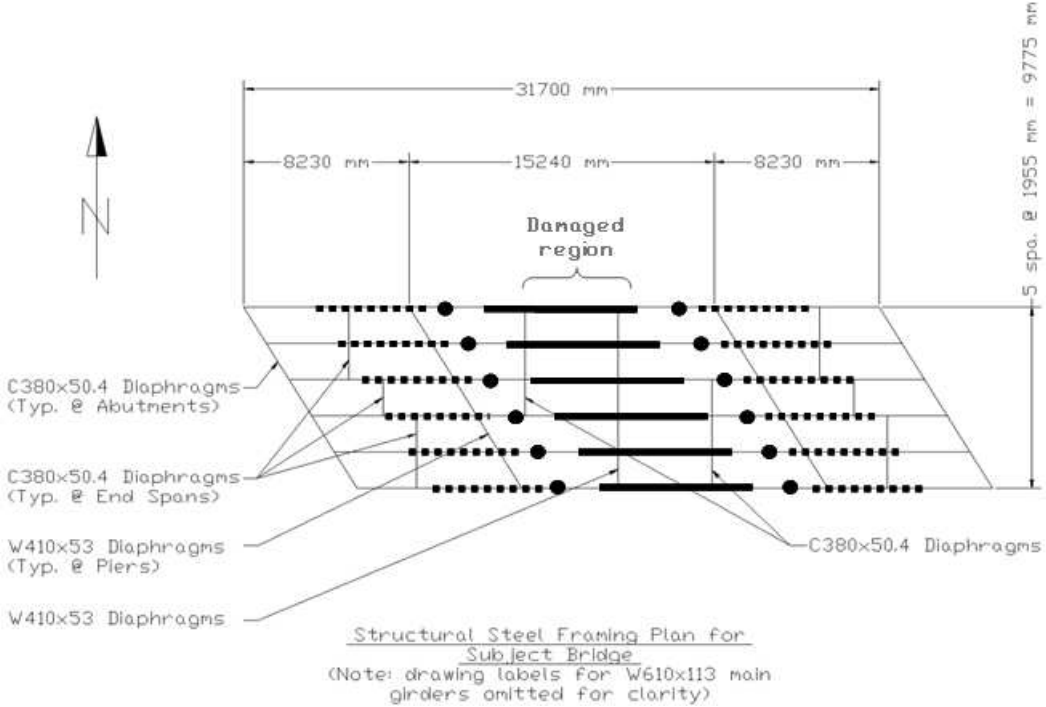


Figure 1.8: Structural steel framing plan for subject bridge.

Transverse diaphragms consist of two typical sections: W410x53 and C380x50.4. The locations of these members are depicted in Figure 1.8. Other important structural features include the presence of three sets of top and bottom flange cover plates, located on each longitudinal steel girder; the thicknesses of all cover plates are 17 mm. One set, indicated by the bold lines in Figure 1.8, consists of 7925 mm cover plates, positioned over the longitudinal centerline of the bridge. Each of the other two sets, indicated by the dashed lines in Figure 1.8, consist of 6095 mm cover plates, located at a 1525 mm outward offset from each pier (away from the center of the bridge). Finally, each of the six girders also has two splice locations that are offset 2285 mm inward from each pier (toward the

center of the bridge); these are indicated by black circles in Figure 1.8.

Bearing conditions consist of genuine pinned connections at the west end of the bridge, (Abutment 1) and rocker-type bearings at each of the two piers and the east end abutment (Pier 1, Pier 2, and Abutment 2, respectively). Typical concrete abutment details, as well as hammerhead-style concrete piers, describe the exposed components of the sub-structure. As it is the steel super-structure that constitutes the primary focus of the research discussed herein, these components from the sub-structure are of little significance, and thus will not be discussed further. The design drawings provided for the subject bridge are dated in the late 1950's, which subsequently motivates the following material specifications. ASTM A7 steel (minimum yield strength of 206.9 MPa) is specified for all structural steel, and the deck concrete is specified by the drawings to have a minimum design compressive strength of 20.7 MPa.

## **Damage**

The most extreme damage to the subject bridge is located approximately 6 m east of Pier 1 (Figure 1.8), on the fascia girder, referred to from this point forward as Girder 1. Due to the nature of the impact(s) from over-height vehicles traveling southbound, the bottom flange of the Girder 1 is deformed toward the interior of the structure; a sample of point cloud data from the damage section is provided in Figure 1.9. Furthermore, the westernmost lateral bracing within Span 2 of Girder 1 provided some resistance at the time of the impact(s), thus resulting in the formation of a bulge (Figure 1.6).

While point cloud data of the damaged region of the bridge are accurate,

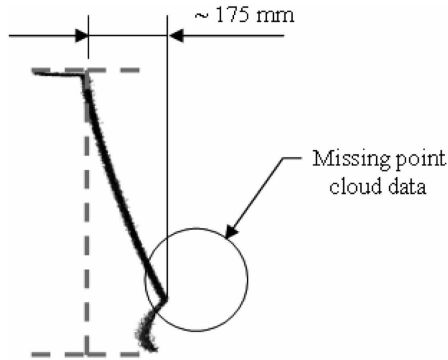


Figure 1.9: Example of point cloud from damaged region of subject bridge.

with respect to the shape of the actual damage, the authors shifted this damaged region to coincide more closely with the midspan of Span 2 of Girder 1. This is done in order to facilitate model construction, in that this shift eliminated interference with transverse diaphragm connections thereby reducing the associated time requirements; such a shift would not typically be employed in the actual application of this bridge assessment methodology.

### 1.3.2 Description of finite element model

The longitudinal steel girders are composed of MITC4 shell finite elements defined along the mid-plane of each of the constituent cross-sectional plate components. The MITC (“mixed interpolation of tensorial components”) formulation employs a mixed interpolation to account for transverse shear strains in such a way as to eliminate the shear-locking phenomenon present in thin, displacement-based shell element formulations [4]. Transverse members are composed of 2-node Hermitian beam elements [80]. These members are rigidly attached to MITC4 shell finite element connector plates, which are subsequently connected to the webs of the longitudinal members. The rigid attachment is

achieved by way of rigid links, which impose a constraint on the applicable degrees of freedom of a “slave” node, such that this node behaves in a kinematically appropriate manner in relation to the displacements of a “master” node. The material models employed for steel cross-sections within this finite element model are as follows: (1) multi-linear inelastic, with properties coinciding with ASTM A7 steel, for all MITC4 shell finite elements; and (2) linear-elastic for all transverse members.

The concrete deck model also employs MITC4 shell finite elements that are offset from the longitudinal steel girders 95 mm (one-half of the concrete deck depth) and connected by way of the node-to-node rigid links. This offset, as imposed by the rigid links, sets these elements in the correct vertical position (i.e. section properties of the composite section are preserved). A multi-linear inelastic material model with an ultimate stress of 20.7 MPa and ultimate strain of 0.003, is employed for the concrete deck, with the addition of a “crack” at the interior pier lines (i.e. element connectivity is eliminated along the line coincident with interior piers). The material model is intended to limit the concrete compressive capacity while the “crack” is intended to account for cracking of the concrete deck in negative moment regions.

### **1.3.3 Results and discussion**

In order to assess the effect of damage on the post-event structure, its response is compared with the baseline case of the undamaged structure. For this portion of the present research, two load configurations are chosen: a uniform deck pressure over the end span, and a uniform deck pressure over each of the three

spans (depicted in Figures 1.10a and 1.10b, respectively). The end span load configuration is employed to develop compression in the bottom flange of the fascia girder. This, in turn, may contribute to a state of lateral instability, which is then exacerbated by the damage (acting as an initial imperfection). The three-span load configuration is employed to develop tension in the bottom flange of the fascia girder, while also engaging the entire structure. While it is expected that this tension will “stretch out” the damaged region, the impact of the damage in the earlier stages of loading is also of interest.

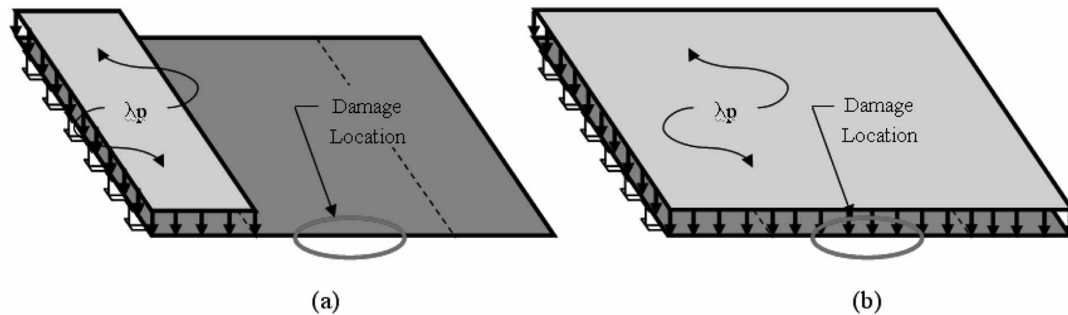


Figure 1.10: (a) End span; and (b) Three span uniform deck pressure load configurations.

The parameter,  $\lambda$ , depicted in Figures 1.10a and 1.10b is termed the “load-proportionality factor” and acts as a scalar multiplier of a reference pressure,  $p$ . This parameter, together with various displacement measures, is used as a means for comparison of the response of the damaged subject bridge to its undamaged counterpart. Justification for this follows from the verification study of the finite element modeling technique employed for the bridge in its undamaged configuration, as conducted by Stull [92].

### End span load configuration

Figures 1.11 and 1.12 provide  $\lambda$ -displacement curves from two points on Girder 1: the midspan location of the loaded end span (Span 1) and the center span (Span 2), respectively. It is expected (and confirmed by Figure 1.13) that Girder 1 will be the location for which the damage has the most significant effect; therefore, corresponding plots of the remaining five undamaged girders will not be necessary. Figure 1.13 provides a contour plot of the difference in vertical displacements at the top-of-steel between the damaged and undamaged bridge, at the final load increment considered for the present research; this provides an indication of the system-wide impact the damage has on the structure. These values are based upon a linear interpolation between the deflections of the top flange-web junction of each girder.

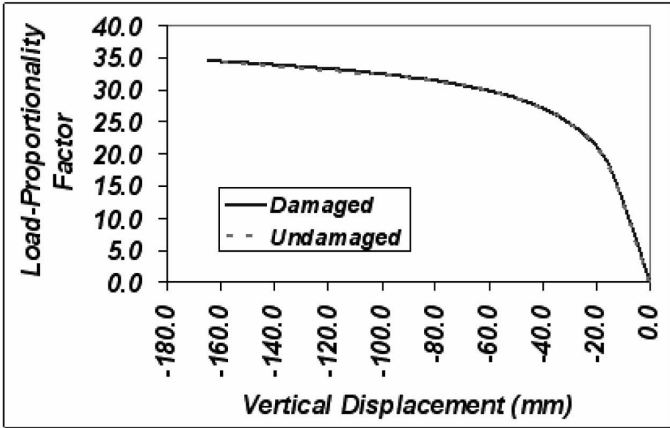


Figure 1.11:  $\lambda$ -displacement plot of midspan of Span 1 for end span load configuration.

Figure 1.11 indicates that the damage to the fascia girder, located within Span 2, has a negligible impact on the midspan deflection of Span 1. When considering Span 2, Figures 1.12 and 1.13 demonstrate some difference in behavior between the damaged and undamaged models.

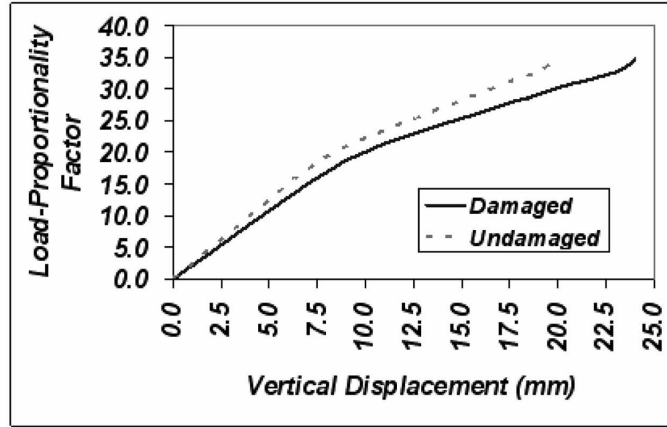


Figure 1.12:  $\lambda$ -displacement plot of midspan of Span 2 for end span load configuration.

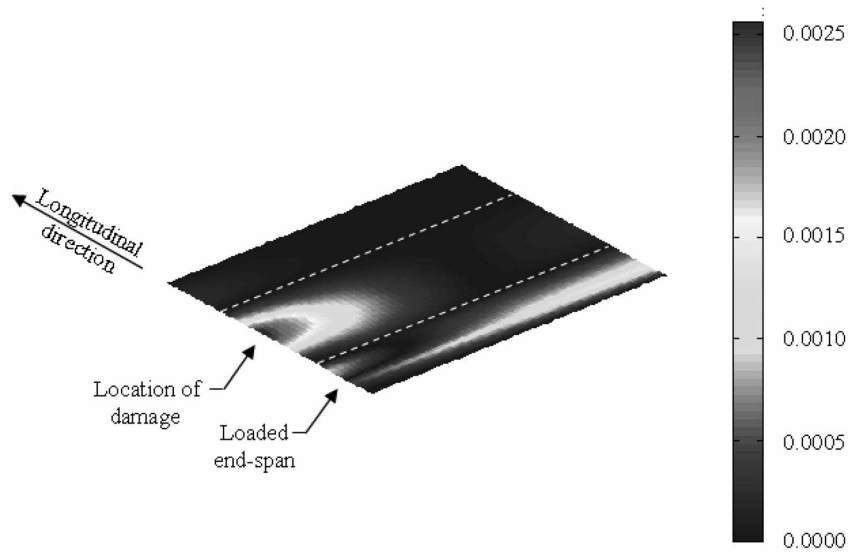


Figure 1.13: Percent difference in top-of-steel deformation between damaged and undamaged models for end span load configuration.

### Three span load configuration

Plots corresponding to those provided for the end span load configuration are also provided for the three-span load configuration (see Figure 1.10b). At the initial stages of loading, there is a significant difference between the behaviors exhibited by the damaged and undamaged models, which becomes most ex-

treme at the transition between the two “linear” portions of the plots (Figures 1.14, 1.15, 1.16). As loading progresses, the differences between the two models diminish to the point where the behaviors coincide. This results from the fact that the load configuration places the damaged region in tension, which in turn “stretches out” the damage to a point where its effect is negligible (Figure 1.17).

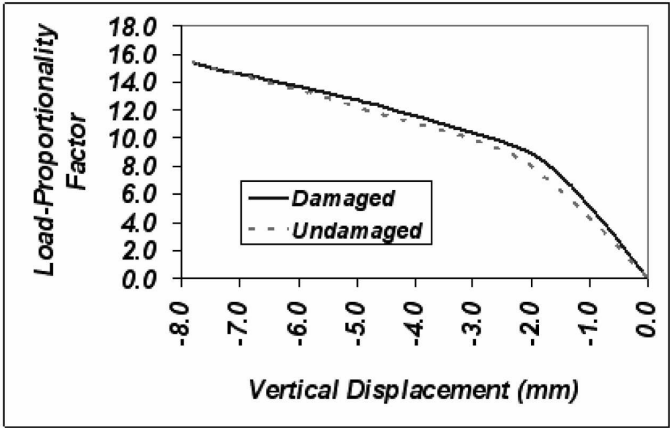


Figure 1.14:  $\lambda$ -displacement plot of midspan of Span 1 for three span load configuration.

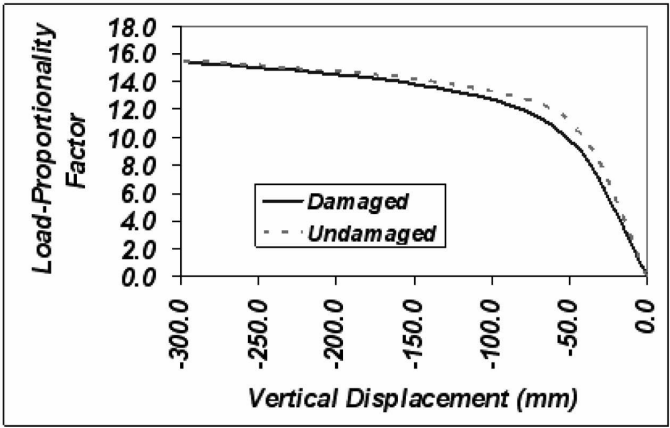


Figure 1.15:  $\lambda$ -displacement plot of midspan of Span 2 for three span load configuration.

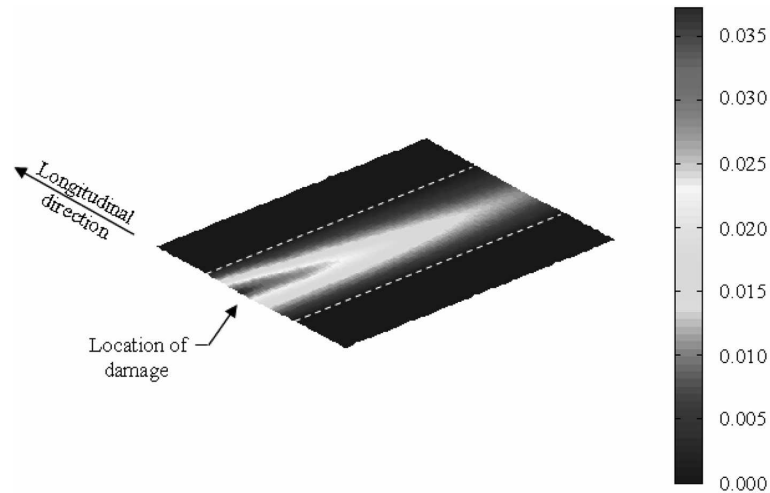


Figure 1.16: Percent difference in top-of-steel deformation between damaged and undamaged models for three span load configuration.

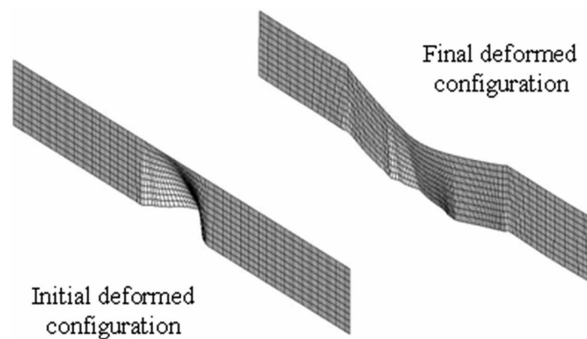


Figure 1.17: Initial and final deformed configurations of the web for three-span load configuration (not to scale).

## 1.4 Conclusions

The results from a research program, aimed at the development of a rapid assessment methodology for bridge structures damaged by truck strikes, have been presented. This research was motivated by the fact that the analysis procedures used in current practice often provide results that may be somewhat subjective. As a result, analyses regarding reserve capacity in damaged bridges may vary significantly between engineering offices.

The approach discussed herein provides a robust and useful technique for assessing both the response characteristics of a damaged structure, as well as its associated reserve capacity. Currently, this technique is not able to be implemented in a truly automated fashion; significant expertise on the part of the analyst is required. While the challenges imposed by the issues discussed in Section 1.2 are significantly lessened by parsing out the damaged region of the bridge, many of these challenges will still present themselves within application contexts. This research program seems to show promise as means for rapidly assessing damaged bridge structures. However, it has been shown herein that a considerable effort on the part of knowledgeable engineers, possessing background in surveying, laser scanning, image processing, and computational mechanics, is required.

## **Acknowledgements**

The Commonwealth of Pennsylvania Department of Transportation is acknowledged for partial support of this work. The views and opinions expressed here are solely those of the authors.

## CHAPTER 2

# *A POSTERIORI* INITIAL IMPERFECTION IDENTIFICATION IN SHELL BUCKLING PROBLEMS<sup>1</sup>

### **Abstract**

The current research seeks to demonstrate that an inverse solution approach, leveraging nonlinear finite element analysis with a divide and conquer type stochastic search algorithm, can identify the presence of localized denting imperfections in cylindrical shell structures. This imperfection field identification is achieved using rather sparse displacement measurements taken at safe, service loading conditions. Both the existence and nature of the imperfection field present in a given shell structure instance are determined. These inferred imperfections are subsequently used to make reasonably accurate predictions regarding the actual shell structure strength at ultimate loading.

### **2.1 Introduction**

A recent and comprehensive survey of research developments during the period 1996 to 2006 [31] highlights the fact that understanding the nature and effects of imperfections in shell structures continues to be a fertile line of inquiry to this day. Since the publication of Koiter's seminal dissertation in 1945, it has become well known that initial imperfections in shell structures may lead to

---

<sup>1</sup>CHRISTOPHER J. STULL, CHRISTOPHER J. EARLS, WILKINS AQUINO. *A POSTERIORI INITIAL IMPERFECTION IDENTIFICATION IN SHELL BUCKLING PROBLEMS*. *COMPUTER METHODS IN APPLIED MECHANICS AND ENGINEERING*, 198(2):260-8, 2008.

dramatic erosions in ultimate strength [11, 37, 90]. However, the jump from this notional understanding, to the realization of a practically useful means for predicting the actual strength of in-service imperfect shell structures, is formidable. It is virtually impossible to rationally guess the precise imperfection field that may be manifest in a given structure; and thus it is problematic to know the buckling strength of this same structure.

The current research aims to address this issue through the development of a method that leverages stochastic search algorithms and nonlinear finite element analysis, in order that relatively sparse sensor telemetry, related to structural response measures (*e.g.* displacement and load intensity), may be used in the solution of an inverse problem that characterizes the initial imperfection field. This *a posteriori* determination of the shell initial imperfection field is made under the safe condition of service loading, but it enables the assessment of the ultimate strength in a given shell structure.

### **2.1.1 Background**

It is well known that experimentally observed buckling loads (or critical loads) for shell structures exhibit considerable scatter, when compared with theoretical predictions [11, 89, 90, 31]. It is commonly assumed that the presence of initial displacement fields, causing deviations from the perfect shell geometry, are the primary cause of this scatter. Contributions from other sources of imperfection, related to boundary conditions, material properties, and shell thickness, are also important to consider [76, 77]. However, given the pronounced effect that initial displacement fields have on the critical load (or buckling load) of

shell structures [89, 90], the present discussion will be restricted in scope to this type of shell structure imperfection.

As it is that there is no completely general shell buckling theory [11] that can be readily applied without considerable specialization for a particular case [27], the nonlinear finite element method enjoys a position of prominence in shell buckling analysis. A frequently adopted strategy for including the effects of geometrical imperfections in shell finite element analyses is to seed the finite element mesh with some scaled approximation to the first buckling mode of the given shell structure [31, 37, 55]. Indeed, most user manuals for commercial software suggest this approach when analyzing such structures. Within this context, a linearized eigenvalue buckling analysis [43] is initially carried out to arrive at an approximation to the first buckling mode [53]. This approximate mode is then scaled using design rules of thumb in order to furnish an asymptotic response that is considered to be representative of the actual, imperfect shell structure under consideration.

Unfortunately, the formerly described approach is neither robust nor reliably accurate. The buckling formulation used, as well as the underlying numerical implementation, can have a very important effect on the nature of the predicted first mode [54, 30]. In addition, there is considerable evidence to show that for many shell structures, it is not the first mode that controls the post-buckling response at unloading [31, 37, 55]. While the error in applying this approach is very problem specific, Featherston [37] has observed errors approaching fifteen percent (either conservative or unconservative errors are possible) in the case of curved shell panels under combined compression and shear.

While there are guidelines and predictive capacity equations for the de-

sign of new shell structures promulgated by various organizations and entities around the world (*e.g.* the German DIN 18800, Eurocode 3, Part 1.6, *etc.*), application of such provisions to analysis problems are fraught with problems and pitfalls as a result of the considerable use of approximation and semi-empirical underpinnings in these methods [79]. More careful approaches to the design problem have become possible through the compilation of measured imperfection fields in the laboratory (as well as in the field) into an *International Imperfections Data Bank* [3]. This repository of shell imperfection data has proven useful in enabling more sophisticated approaches to design. For instance, an artificial neural network (ANN) has been trained using results from 33 of the experiments contained within the data bank. These experiments pertained strictly to cylindrical shells, but the ANN's favorable predictive ability (*i.e.* an average error of 1.6 percent and a maximum observed error of 5.2 percent) indicates the promise of the approach [100].

For the purposes of design, consideration of shell structure imperfection sensitivity within a stochastic framework, leveraging the data bank [3] has shown great promise [76, 77, 13]. Bielewicz and Gorski [13] have applied standard Monte Carlo methods to generate imperfection fields that are consistent with experimentally measured results [3]. Nonlinear finite element analysis is subsequently applied by these authors, as the means for ascertaining the shell structural response to the given imperfection field. Reliability estimates may then be made using loading statistics in combination with numerically obtained response statistics.

A more sophisticated approach to the stochastic consideration of shell imperfections is provided by Papadopoulos and Papadrakakis [76, 77]. In their

work, a stochastic finite element approach, based on a spectral description of the random fields and a stochastic stiffness matrix, is used to compute a histogram of the critical buckling load of cylindrical shell panels. In these earlier studies [76, 77], the notion of an imperfection encompasses initial displacements, as well as material and thickness variations. Related, and complementary work pertaining to cylindrical shells with cutouts can be found in [86], where the effects of random geometric imperfections on the critical load are studied.

The work of El Damatty and Nassef [32] takes a different approach to the treatment of the design problem. In their work, El Damatty and Nassef apply Genetic Algorithms (GA), in conjunction with nonlinear finite element analysis techniques, in order to arrive at the worst case imperfection fields for various conical shell structure geometries. The fitness function of the GA takes the critical load as the parameter to be solved for, and thus a hypothetical design space is searched for the imperfection field that minimizes the critical load of the shell structures under consideration.

The present work is concerned with the development of a method that employs sparse sensor telemetry, acquired during a safe service loading condition, for use in the solution of an inverse problem that characterizes the actual, and previously unknown, imperfection field in a shell structure. This *a posteriori* determination of the shell initial imperfection field is then used to make strength predictions regarding the shell structure in question. The method utilizes geometrically nonlinear finite element forward models, in conjunction with stochastic search methods employing Genetic Algorithms to solve the system identification inverse problem related to the initial imperfection field. This identified field is subsequently used in the forward model to make strength

prognoses regarding the structure.

### **2.1.2 Paper organization**

A discussion of issues concerning the forward and inverse problem formulations related to the current research is given in Section 2.2 of the current paper; while Section 2.3 discusses salient features regarding the solution of a particular forward and inverse problem associated with edge supported barrel vault shells. Section 2.4 presents results from the inverse solutions, and provides context in the form of a discussion, in order that conclusions may be drawn in Section 2.5.

## **2.2 Problem formulation**

### **2.2.1 Forward problem**

In developing the forward and inverse problem formulations, three domains will be defined coincident with three distinct configurations (Figure 2.1):  $\Omega_o$  representing the perfect body;  $\Omega'$  resulting from the imposition of an initial imperfection field,  $\tilde{u}_o$ ; and the final configuration assumed by the imperfect body upon application of external loading,  $\Omega$ . The respective boundaries of these three domains are denoted by  $\partial\Omega_o$ ,  $\partial\Omega'$ , and  $\partial\Omega$ . The forward problem consists of finding the displacement field  $\tilde{u}'$  given: the domain  $\Omega_o$ ; the initial imperfection field,  $\tilde{u}_o$ ; a material constitutive model; and an adequate set of boundary conditions. The boundary value problem describing this forward problem

is given in Box (2.1) (assuming static loading and no mass transfer across the boundary.)

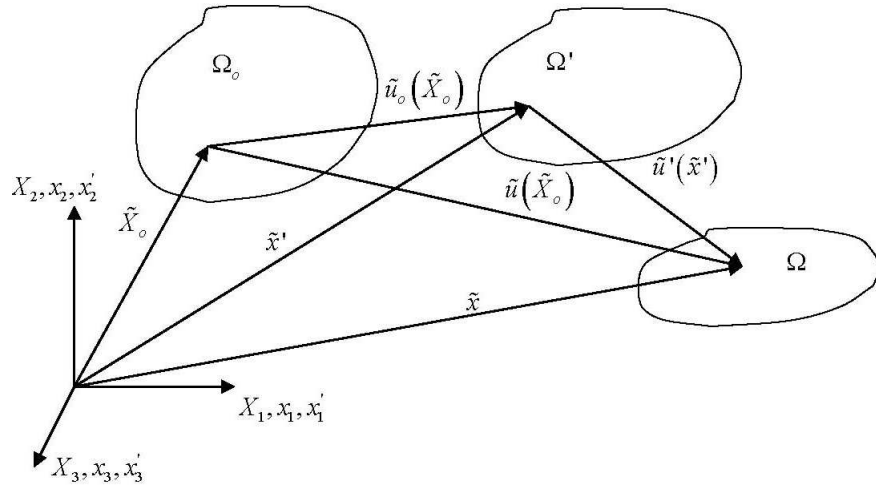


Figure 2.1: Configurations for forward and inverse problems.

$$\nabla \cdot \boldsymbol{\sigma} = \tilde{\mathbf{0}} \text{ in } \Omega$$

$$\boldsymbol{S} = \boldsymbol{C}^{IV} : \boldsymbol{E}$$

$$\boldsymbol{S} = | \boldsymbol{F} | \boldsymbol{F}^{-1} \boldsymbol{\sigma} \boldsymbol{F}^{-T}$$

$$\boldsymbol{\sigma} \tilde{\boldsymbol{n}} = \tilde{\boldsymbol{\tau}} \text{ on } \partial\Omega_N$$

$$\tilde{\boldsymbol{u}} = \tilde{\tilde{\boldsymbol{u}}} \text{ on } \partial\Omega_E$$

$$\Omega' = \{ \tilde{\boldsymbol{x}}' : \tilde{\boldsymbol{x}}' = \tilde{\boldsymbol{X}}_o + \tilde{\boldsymbol{u}}_o \}$$

$\boldsymbol{\sigma}$  Cauchy stress tensor

$\boldsymbol{S}$  Second Piola–Kirchhoff stress tensor

$\boldsymbol{E}$  Green–Lagrange strain tensor (2.1)

$\boldsymbol{F}$  deformation gradient going from  $\Omega'$  to  $\Omega$

$\boldsymbol{C}^{IV}$  fourth order elasticity tensor

$\tilde{\boldsymbol{n}}$  unit vector normal to the boundary  $\partial\Omega_N$

$\tilde{\boldsymbol{\tau}}$  traction vector

$\partial\Omega_N$  portion of boundary where Neumann (*i.e.* natural) conditions  
are prescribed

$\partial\Omega_E$  portion of boundary where Dirichlet (*i.e.* essential) conditions  
are prescribed

In this work, vectors will be denoted with a tilde on top, tensors will be represented with bold letters, column matrices will be denoted with curly braces, and all other matrices will be presented with square brackets.

A general updated Lagrangian finite element formulation of the boundary

value problem provided in Box (2.1) is presented in Box (2.2). For more details on this formulation see [12].

$$V(\Omega') = \{\tilde{w}(\tilde{x}') : \tilde{w} \in H^1(\Omega'), \tilde{w} = 0 \text{ on } \partial\Omega'_E\}$$

$$U(\Omega') = \{\tilde{u}'(\tilde{x}') : \tilde{u}' \in H^1(\Omega'), \tilde{u}' = \tilde{u}'(\tilde{x}') \text{ on } \partial\Omega'_E\}$$

Weak form:

$$0 = \int_{\partial\Omega'_N} \tilde{w} \cdot \tilde{\tau} da - \int_{\Omega} \nabla \tilde{w} : \sigma dv$$

Finite element–discretized weak form:

$$\{0\} = \{I\} - \{P_{ext}\}$$

$$\{I\} = \sum_{elements} \int_{\Omega^e} [B]^T \{\sigma\} dv^e \quad (2.2)$$

$$\{P_{ext}\} = \sum_{elements} \int_{\partial\Omega_N^e} [N]^T \{\tau\} da^e$$

$V(\Omega')$  space of test functions

$U(\Omega')$  space of trial functions

$H^1(\Omega')$  Sobolev space

$[N]$  matrix containing element shape functions

$[B]$  matrix containing derivatives of shape functions

$\Omega^e$  element domain

## 2.2.2 Inverse problem

In the inverse problems formulated in the current work, the primary unknown is the initial imperfection field,  $\tilde{u}_o$ . It will be assumed that the perfect configuration,  $\Omega_o$ , is known, and partial information about the deformed current configuration,  $\Omega$ , has been observed (*i.e.* measured).

Consider a collection of observations, or measurements, in the current configuration denoted by

$$U_{obs} = \{\tilde{u}'_{obs}(\tilde{x}') : \tilde{x}' \in \Omega'\} \quad (2.3)$$

and a set of predictions computed through the solution of the forward problem shown in Box (2.1), and defined as

$$U_M(\tilde{u}_o) = \{\tilde{u}'_M(\tilde{x}', \tilde{u}_o) : \tilde{x}' \in \Omega'\} \quad (2.4)$$

The inverse problem is subsequently cast as an optimization problem whose objective functional has the form:

$$J(\tilde{u}_o) = \| U_{obs} - U_M(\tilde{u}_o) \| \quad (2.5)$$

where  $\| \cdot \|$  is an adequate metric that quantifies the distance between given sets.

The subsequent optimization problem appears as

$$\min_{\tilde{u}_o(\tilde{X}_o) \in H^1(\Omega')} J(\tilde{u}_o) \quad (2.6)$$

Notice that the foregoing optimization problem deals with an infinite dimensional space since the main unknown is  $\tilde{u}_o(\tilde{x}')$ . In this work, a finite dimensional representation of the initial imperfection field is proposed. This finite dimensional representation is made with the intention to treat localized geometric imperfections within the problem domain (*i.e.* the presence of denting).

Such localized effects may arise in aircraft fuselage structures as a result of inadvertent contact during servicing (*e.g.* dropping a tool), within the hulls of ships damaged by collision, *etc.* The point here being that a common problem seems to be in determining what damage may have been done; and what effect will it have on future performance.

A natural approach for simulating a dent involves the use of Gaussian Radial Basis Functions (RBFs) [48]. The use of RBFs allows for a convenient parameterization of the initial imperfection field; subsequently facilitating the use of stochastic search algorithms (*e.g.* Genetic Algorithms, Simulated Annealing, *etc.*) for the solution of the inverse problem. A parameterized initial imperfection field is given as:

$$\tilde{u}_o \approx \sum_{i=1}^N \{\omega\}_i \Psi_i(\tilde{X}_o) \quad (2.7)$$

where

$$\Psi_i(\tilde{X}_o) = e^{-\left(\frac{\|\tilde{c}_i - \tilde{X}_o\|_{\ell_2}}{\sqrt{2}\sigma_i}\right)^2} \quad (2.8)$$

is a Gaussian RBF in which  $\tilde{c}_i$  represent the radial basis centers and  $\sigma_i$  are their standard deviations, and  $\{\omega\}_i$  are the Fourier coefficients of the initial imperfection approximation. These variable will be treated as the primary unknowns in the inverse problem. Introducing a column matrix that gathers all the unknowns as

$$\{\alpha\} = \begin{Bmatrix} \tilde{c}_1 \\ \{\omega\}_1 \\ \sigma_1 \\ \vdots \\ \tilde{c}_n \\ \{\omega\}_n \\ \sigma_n \end{Bmatrix} \quad (2.9)$$

the inverse problem becomes a parametric optimization problem, expressed as

$$\min_{\{\alpha\} \in \mathbb{R}^q} J(\{\alpha\}) \quad (2.10)$$

Here the dimension of the column matrix,  $\{\alpha\}$  is  $q = n \times (2 \times nsd + 1)$ , where  $nsd$  is the number of spatial dimensions, and  $n$  is the number of basis functions used in the approximation of the imperfection field.

### 2.3 Model problem

The foregoing formulations may be specialized for application to a model problem. Thus, the discussion now turns to describing the approaches taken in the forward solution of a model problem, in order to obtain simulated experimental results that are used to glean a set of so-called *observed* data from a problem with a known initial imperfection. These data are subsequently compared with forward modeling results emanating from imperfect shell geometries obtained using a stochastic search algorithm. Stochastic search algorithms prove useful in the model problems considered herein; each of which displays complex, non-convex objective functions (as surmised from the examination of objective function evaluations carried out at multiple random points within the problem domain). Stochastic search methods have proven useful in finding the global minimum in such spaces [68, 46, 49].

The model problem geometry considered in the current work is displayed in Figure 2.2. This model problem is the basis for all results presented in the sequel. The selection of a portion of a cylindrical shell, with the associated pinned boundaries, was made in order to enhance imperfection sensitivity [31]. The present research intends to demonstrate a means for inferring the presence of an

initial imperfection field within the shell domain, to characterize it in a quantifiable way using service loading response, and then to subsequently make prognoses regarding the overall shell buckling strength. In light of these aims, it is important to address the type of imperfections being considered in this work.

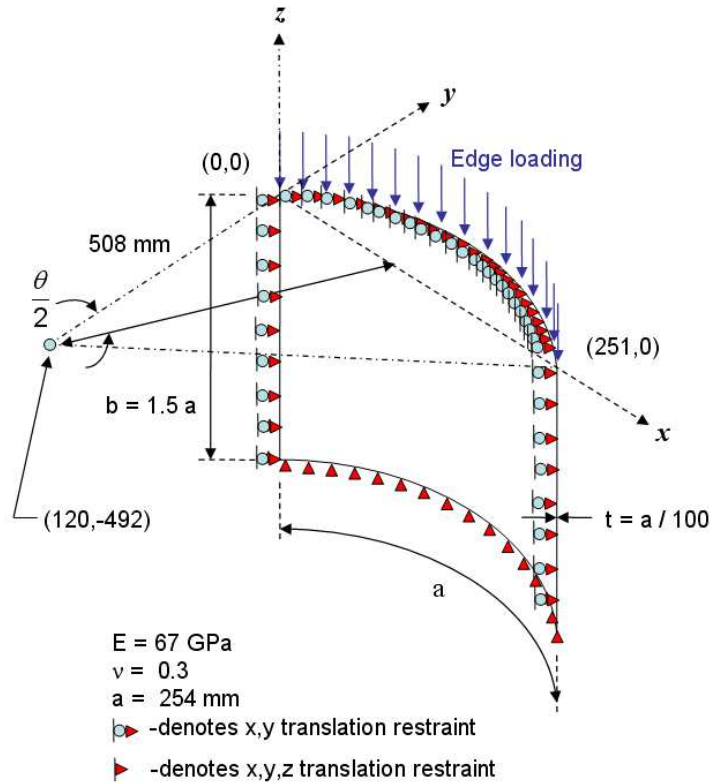


Figure 2.2: Edge loaded barrel vault shell example structure.

As dents are the focus of the current work, Gaussian Radial Basis Functions (RBFs) [48] are employed as a convenient means for parameterization of the initial imperfection field; subsequently facilitating the use of stochastic search algorithms for the solution of an inverse problem aimed at identifying the approximate form of the initial imperfection field within the model problem domain.

A representative form of a Gaussian RBF is given in Equation (2.8). A sub-

sequent approximation to the initial imperfection field,  $\tilde{u}_o(\tilde{X}_o)$ , may be given using Fourier coefficients,  $\omega_i$  [82]:

$$u_o(\tilde{X}_o) \approx \sum_{i=1}^N \omega_i \Psi_i(\tilde{X}_o) \quad (2.11)$$

where an  $\omega_i$  of unity corresponds to an RBF with a height of 25.4mm, for the model problem described in Figure 2.2. A depiction of a single Gaussian RBF, superimposed on the model shell problem, is displayed in Figure 2.3. Within the model problems, each particular dent will correspond with its own RBF (*i.e.* in the case of two dents, each will be represented by its own, single RBF). These model problems will serve as the *observed* case (*i.e.* a surrogate for an experimentally observed instantiation of the shell).

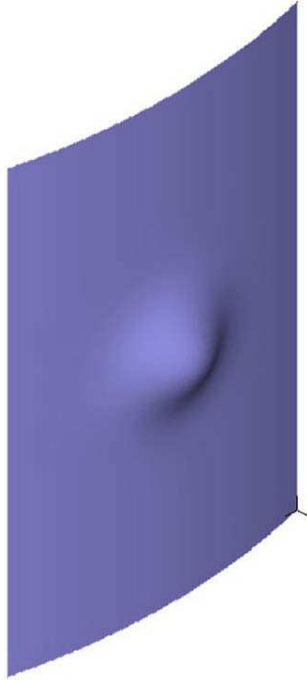


Figure 2.3: Representative dent imperfection (magnified 1000×).

### 2.3.1 Forward modeling

The forward modeling of the shell structure depicted in Figure 2.2 is carried out within the context of the nonlinear finite element method (geometric nonlinearity only). Specifically, the four node, assumed strain, shell finite element given by Bathe and co-workers (*i.e.* MITC4 Shell) [29, 6, 7] is employed in conjunction with the classical Newton–Raphson solution approach [62]. A detailed mesh convergence study carried out for collapse of the model problem (see Figure 2.4 for a summary of these results) reveals that a MITC4 mesh with approximately 200,000 degrees of freedom represents a very accurate mesh; suitable for use as the *observed* case within the context of the current inverse problem solution. A much less dense mesh (having approximately 50,000 degrees of freedom) is thought to represent a reasonable compromise between modeling accuracy and computational expedience; and thus this mesh is used in conjunction with the stochastic search algorithm (as the *measured* case).

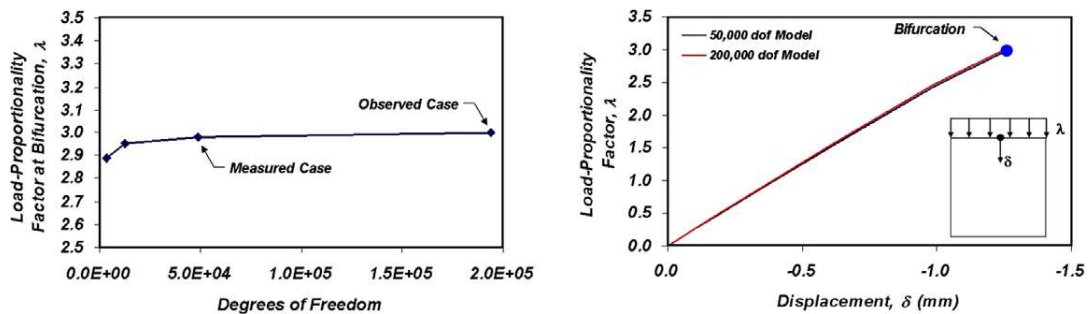


Figure 2.4: Summary of mesh convergence study results.

The large number of analyses that are required for the solution of this type of inverse problem (*i.e.* potentially thousands of runs of the forward model) justifies the tradeoff in accuracy for solution speed. It is pointed out that while the standard Newton–Raphson nonlinear solution algorithm is used in the so-

lution of the inverse problems, a hybrid solution algorithm, combining a modified spherical arc length method and the constant increment of external work method [5], is used in the collapse analyses associated with the mesh convergence study. It is further noted that imperfect meshes were used in the conduct of the above mentioned convergence study; as per [78]. An approximation to the first global buckling mode, as obtained from a linearized eigenvalue buckling analysis, was employed as a means for perturbing the mesh geometry used during the nonlinear collapse analyses.

### 2.3.2 Inverse solution

A grid of sixteen uniformly spaced sampling points is superimposed on the shell surface of the model problem. Displacements along the direction of the normal to the undeformed shell surface are stored after the application of a service load, that is approximately seventy percent of the critical load. In the case of the fine mesh model (*i.e.* the mesh with approximately 200,000 degrees of freedom), these data become the *observed* case response. The same sixteen sample point locations are also applied to the coarser meshes (*i.e.* those with approximately 50,000 degrees of freedom) in order to capture a comparable displacement field in the shell normal direction. In this latter case, different initial imperfection fields are identified by the stochastic search algorithm, and their agreement with the *observed* case is subsequently determined using the objective function given in Equation (2.12):

$$J(\{\alpha\}) = \frac{1}{\|\{u'_{obs}\}\|_{\ell^\infty}} \sum_{n=1}^{16} |(u'_{obs})_n - (u'_M)_n| \quad (2.12)$$

where  $(u'_{obs})_n$  are the normal components of the displacement vectors, with respect to configuration  $\Omega'$ , in the *observed* case; taken at sixteen uniformly spaced sampling locations within the mesh. Similarly,  $(u'_M)_n$  are the analogous displacements obtained from the models prescribed by the stochastic search algorithm; the so-called *measured* case.

### **Genetic algorithm**

As mentioned previously, a stochastic search algorithm is applied in this research because the more computationally efficient gradient-based approaches cannot adequately address the occurrence of multiple minima that accompany the complex objective functions associated with the current problem types. Specifically a Genetic Algorithm (GA) is the stochastic search method adopted in this work. GAs have proven useful, as an alternative to gradient-based optimization algorithms, in instances where objective functions are non-convex [46, 49].

GAs emulate aspects of biological evolution, in their reliance on three fundamental principles: heredity; mutation; and natural selection [23, 47]. In the natural world, individuals with favorable traits for survival persist long enough to transmit those traits to the next generation through the process of reproduction. Random mutation occurs slowly and sporadically, as a mechanism whereby new traits are introduced into a population. Traits that are favorable, from the standpoint of survivability, are retained; since they enable the individuals so endowed to succeed against survival pressures and reproduce. The converse is also a very powerful agency in the process [23].

In the case of GAs, the objective function (*i.e.* Equation (2.12)) provides the selection pressure to judge *fitness*; while *cross-over* and *elitism* furnish the mechanisms for reproduction. Spurious genetic variations are introduced into the GA through the mechanism of *mutation*. Many different general approaches for the implementation of the foregoing GA components are discussed in the literature [46, 49, 68]. The discussion now shifts to the particulars associated with the form of the GA used in the current work.

While it has already been mentioned that the objective function presented in Equation (2.12) furnishes the selection pressure, the details of reproduction and mutation require elucidation. In this work, the individual RBF parameters are represented by the genes comprising the chromosome of each individual. Instances of a given chromosome essentially describe a particular individual to be sent to the forward model, and subsequently assessed in term of fitness using Equation (2.12).

Depending on the number of dents and RBFs, the number of individuals in a particular generation can range from 22 (for single dent with 1 RBF in a single quadrant) to 128 (for double dent with 4 RBFs searching over all four quadrants); as a result of the need to search over the four parameters associated with each particular RBF used in the imperfection field approximation. After all runs of the forward solver have been carried out on the individuals making up a particular generation, the top two are retained, unaltered, and projected into the next generation (*i.e.* this is the notion of *elitism*). The top eighty percent of the remaining individuals are permitted to reproduce through the mechanism of *single point cross-over*. In this way, a single point in the chromosomes of two randomly selected individuals (*i.e.* selected with stochastic uniform sam-

pling), from within the cross-over population, are identified. These two individuals trade chromosome segments, as delineated by the randomly selected cross-over marker; all the while preserving the original chromosome length. In addition, the least fit individuals in the given population (*i.e.* those not permitted to reproduce) are selected to experience a random mutation of individual genes in their chromosome. Such mutation has a probability of occurrence of 0.10; the subsequently mutated individuals from this population are projected forward into the next generation to compete for survival once again. It is the aspects of reproduction in general, and mutation in particular, that facilitate the treatment of the complex, non-convex objective functions that accompany our model problem.

Indeed, the objective functions prove so complex that conventional approaches to GA searching do not always perform satisfactorily with regard to reasonable wall clock times for the solution of the inverse problem. As a result of this complexity, a *divide and conquer* like approach is employed in the GA methods used herein. This approach is essentially heuristic, in that it proceeds in a seemingly natural way, given the projection of the model problem onto  $\mathbb{R}^2$  describes a rectangular domain. Specifically, the problem domain of the shell, depicted in Figure 2.2, is separated into four quadrants. Within each quadrant, the vertex that coincides with a vertex in the actual global problem domain (subsequently referred to as simply the *vertex*) serves as a point of reference for guiding the stochastic search over the RBF centers,  $\bar{c}_i$  (see Equation (2.8)). A truncated Gaussian probability density function (PDF), centered on the vertex, favors searching in the vicinity of the vertex by controlling the probability associated with the position of the RBF center in the mutated individuals, relative to the quadrant vertex (see Figure 2.5). In this way, early instances of

mutations in the positions of RBF centers emphasize locations that are close to the vertices; while in later solution times, the radius of emphasis is expanded to encompass the entire model problem domain (*i.e.* all four quadrants). In other words, as the solution time grows, the variance of the truncated Gaussian PDF is increased; thus permitting more of the domain to be accessed by the RBF centers. It is pointed out that the truncated Gaussian PDF is used to guide the search over the RBF centers, only. The variation over the other RBF parameters in Equation (2.8) (*i.e.*  $\sigma_i$  and  $\omega_i$ ) follows a standard uniform distribution, summed with the mid-point of the interval associated with the individual variable ranges.

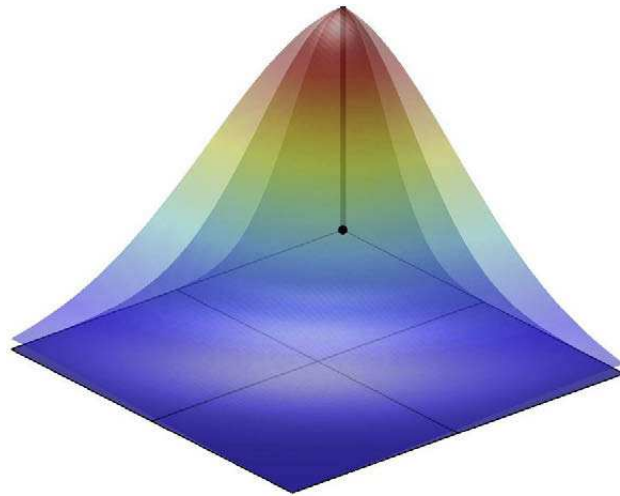


Figure 2.5: Truncated Gaussian PDF used to mutate RBF centers away from vertices.

The final populations from the individual searches over all four quadrants are subsequently combined into a single population for a final search over the entire problem domain (with no further emphasis on the vertices). The shell imperfection instantiation emerging from this final search, with the smallest value of Equation (2.12), is identified as the solution of the inverse problem. Figure 2.6 provides a schematic depiction of the foregoing divide and conquer stochastic

search approach.

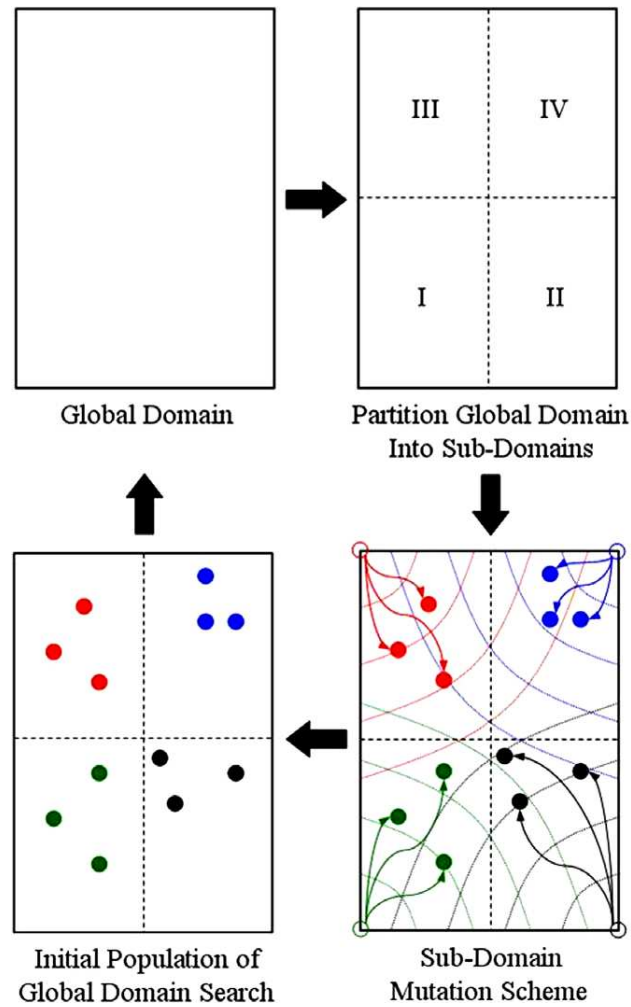


Figure 2.6: Schematic depiction of stochastic search approach.

The salient features of the individual GAs used in the current work are provided in the following listings.

Single RBF case:

*(analyses emphasizing single quadrants)*

- 30 generations of 22 individuals
- 2 elite individuals are employed

- single point cross-over, using eighty percent of the non-elite individuals
- mutation rate for each gene in a chromosome is 10 percent, in remaining 20 percent of non-elite individuals
- A truncated Gaussian PDF guides mutation of genes coinciding with RBF centers, while all other RBF parameters employ a uniform PDF.

*(final analysis over all four quadrants, using best individuals from single quadrant cases)*

- 30 generations of 32 individuals: with initial population comprised of the top 8 individuals from searches of each of the quadrants
- 2 elite individuals are employed
- single point cross-over, using eighty percent of the non-elite individuals
- mutation rate for each gene in a chromosome is 10 percent, in remaining 20 percent of non-elite individuals
- a uniform probability of gene mutation is employed over all RBF parameters

Four RBF case:

*(analyses emphasizing single quadrants)*

- 30 generations of 88 individuals
- 2 elite individuals are employed
- single point cross-over, using eighty percent of the non-elite individuals
- mutation rate for each gene in a chromosome is 10 percent, in remaining 20 percent of non-elite individuals

- A truncated Gaussian PDF guides mutation of genes coinciding with RBF centers, while all other RBF parameters employ a uniform PDF.

(final analysis over all four quadrants, using best individuals from single quadrant cases)

- 30 generations of 128 individuals: with initial population comprised of the top 32 individuals from searches of each of the quadrants
- 2 elite individuals are employed
- single point cross-over, using eighty percent of the non-elite individuals
- mutation rate for each gene in a chromosome is 10 percent, in remaining 20 percent of non-elite individuals
- a uniform probability of gene mutation is employed over all RBF parameters

It is pointed out that while simulated noise in experimental displacement measurements is not explicitly included in the results from the *observed* case, robustness of the inverse solution method is nonetheless tested in this work. Since the mesh associated with the *observed* case is approximately four times more dense than the meshes considered in the forward models used in the stochastic search, critical differences between these solutions exist in a theoretical sense. These differences rest in the fact that that the theoretical continuous forward modeling solution is being projected onto subspaces with dimensionality of approximately 200,000 and 50,000, respectively, for the *observed* and *measured* cases. The solution differences associated with the variations in solution projection are thought to be sufficient to avoid committing an *inverse crime*.

## 2.4 Results and discussion

As the current paper focuses on identification of initial geometric imperfection fields that are consistent with denting, two scenarios are considered: the case of a single dent located in the middle of the shell (Figure 2.7, left); and the case of two dents located in opposing corners of the shell (Figure 2.7, right). In the case of the double dent configurations, it is pointed out that the dent in the upper right corner has a considerably smaller amplitude, as compared with the dent in the lower left corner (*i.e.* 0.0508 mm versus 0.0127 mm). This difference will be useful to recall in the subsequent discussion on this case.

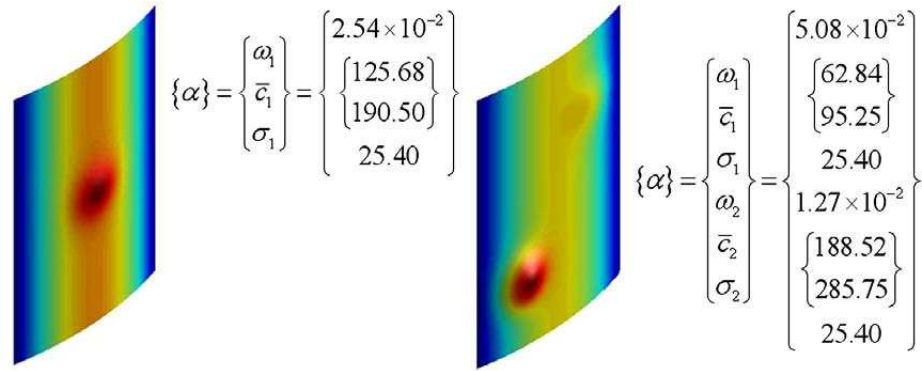


Figure 2.7: Actual initial configurations with associated RBF parameters: single dent on left; double dent on right.

The simplest case to consider is that in which the stochastic search algorithm searches the four dimensional RBF parameter space for the *observed* solution associated with the actual single dent initial imperfection field. As the inverse solution algorithm adopted in this work employs a stochastic search methodology, five distinct solutions are attempted with the single RBF dent representation. A representative inverse problem solution for this case appears in Figure 2.8, while a comparison in agreement, between all five cases and the *observed* case,

is furnished in Table 2.1, using the following discrete norm generated metric:

$$\|\{\delta u_o\}\|_{\ell^2} = \frac{1}{n} \left( \sum_{i=1}^n \left( (u_o)_{obs,i} - (u_o)_{M,i} \right)^2 \right)^{\frac{1}{2}} \quad (2.13)$$

where the variables,  $u_o$ , refer to the normal component of the displacement vectors, measured with respect to the initial configuration  $\Omega_o$ , and taken at locations coinciding with the nodal coordinates from the 50,000 degree of freedom model (*i.e.*  $n = 9,801$ ). In this way a quantitative comparison between the *observed* and predicted imperfections fields is possible.

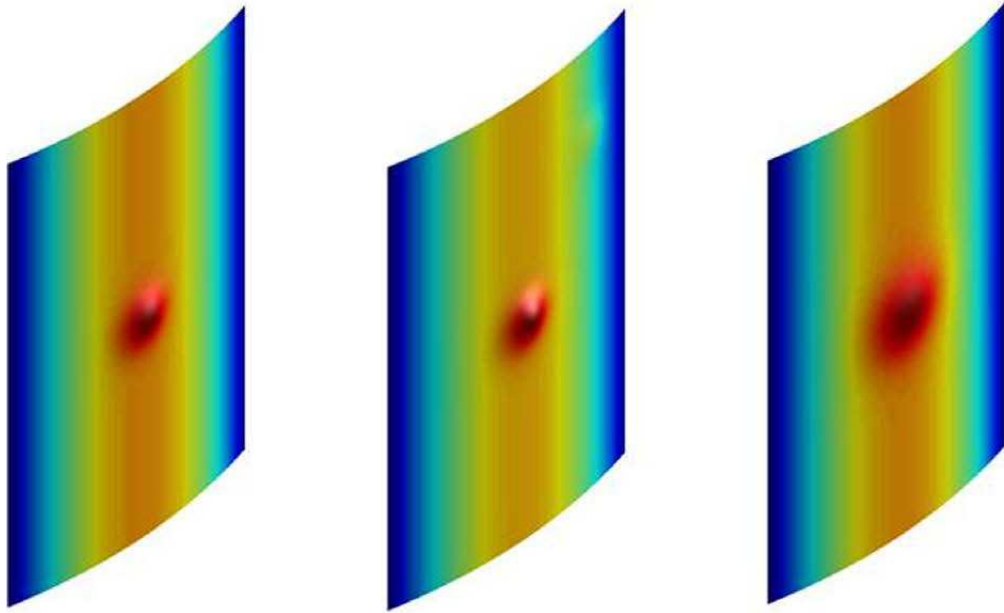


Figure 2.8: Representative single dent solutions using one (left) and four (center) RBFs in inverse solution; actual imperfection on right.

Table 2.1: Comparison of results for representations of single dent with one RBF

Run	$\ \{\delta u_o\}\ _{\ell^2}$
1	1.806E-5 mm
2	1.826E-5 mm
3	2.061E-5 mm
4	1.806E-5 mm
5	1.816E-5 mm

It might be expected [61, 82] that increasing the dimensionality of the approximate solution space being searched should not result in any erosion of the inverse solution quality. Indeed, the consideration of the single dent case with its space of possible imperfection fields spanned by four RBFs furnished very similar results to the single RBF case. A representative depiction of the deformed geometry obtained for the four RBF case is displayed in Figure 2.8; while the accompanying norms,  $\|\{\delta u_o\}\|_{\ell^2}$  appear in Table 2.2.

Table 2.2: Comparison of results for representations of single dent with four RBFs

Run	$\ \{\delta u_o\}\ _{\ell^2}$
1	1.888E-5 mm
2	2.000E-5 mm
3	2.183E-5 mm
4	2.081E-5 mm
5	2.306E-5 mm

In the case where four RBFs were used to represent a single dent in the inverse problem solution, a general observation can be made: one, or more, of the RBFs tend to migrate to the location of the dent, while those that do not, display amplitudes approaching zero. In the case of the migrating RBFs, the sum tended to approach that of the target dent imperfection amplitude. This is, of course, entirely as expected.

In the case of the second example of local imperfections considered (*i.e.* the double dent case), a four RBF representation of the initial imperfection field is considered. Once again, a reasonable agreement is observed between the results from the inverse problem solution, and the results from the *observed* case. Figure 2.9 displays a representative solution of the inverse problem for this case, while Table 2.3 provides a quantitative comparison with the results from the *observed* case, once again employing the norm from Equation (2.13).

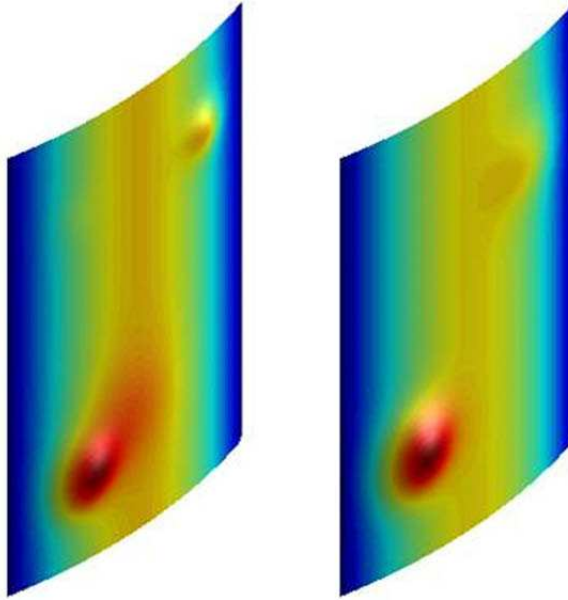


Figure 2.9: Representative double dent solution using four RBFs in inverse solution: approximate imperfection on left; actual imperfection on right.

Table 2.3: Comparison of results for representations of double dent with four RBFs

Run	$\ \{\delta u_o\}\ _{\ell^2}$
1	6.840E-6 mm
2	3.880E-6 mm
3	1.326E-5 mm
4	1.684E-5 mm
5	1.330E-6 mm

It is difficult to draw specific conclusions regarding the nature of the inverse problem results presented in Tables 2.1 through 2.3, as a result of the realities associated with implementation of stochastic searches. Specifically, since it is that considerably more information is present in the four RBF case, as compared with the single RBF case, significantly more solution steps are required in order to permit the space of all admissible solution parameters to be explored. While this general observation is logical to consider, it is not possible to know exactly how many iterations would be needed to permit the precise comparison in the

rates of convergence, to the exact solution, between the cases of one and four RBFs.

Another useful means for comparison of the foregoing results involves the very practical matter of how well the buckling loads from the models incorporating the inversely identified imperfection fields predict the critical loads from the *observed* cases. Tables 4 and 5 furnish such comparison results for the cases of single and double dent imperfections, respectively. In these tables, the relative error is computed as:

$$e_1 = \left| \frac{(LPF_{cr})_{obs} - (LPF_{cr})_M}{(LPF_{cr})_{obs}} \times 100 \right| \quad (2.14)$$

where  $LPF_{cr}$  is the load proportionality factor being applied to a constant reference load vector imposing a total reaction of 71.6 kN along the loaded edge of the model shell problem. Thus the critical loading resultant, for any particular imperfection case, is given as  $(LPF_{cr}) \times (71.6kN)$ . As a result of the inclusion of initial imperfections, the critical load corresponds with the first limit point, rather than a point of bifurcation in the equilibrium path (as would accompany the response of the case with perfect geometry). This critical limit load level is taken to correspond with the last converged equilibrium configuration in the incremental nonlinear finite element analysis, previous to the first increment leading to a non-positive definite system stiffness. Based on the agreement in predictions that are presented in Tables 2.4 and 2.5, it would appear that this approach may have practical value.

It is worth pointing out that in spite of the fact that the objective function from Equation (2.12) exhibited a significantly smaller sensitivity to the presence of the smaller of the two local imperfections (*i.e.* the dent in the upper right corner), the inverse model solutions nearly always predicted the presence of this

Table 2.4: Comparison of single dent buckling results ( $LPF_{cr})_{obs} = 1.869$

1 RBF			4 RBFs		
Run	$LPF_{cr}$	$e_1$	Run	$LPF_{cr}$	$e_1$
1	1.874	0.261	1	1.873	0.236
2	1.874	0.266	2	1.873	0.226
3	1.875	0.300	3	1.872	0.183
4	1.874	0.264	4	1.872	0.190
5	1.874	0.265	5	1.873	0.194

Table 2.5: Comparison of double dent buckling results ( $LPF_{cr})_{obs} = 1.875$

4 RBFs		
Run	$LPF_{cr}$	$e_1$
1	1.872	0.169
2	1.872	0.173
3	1.874	0.040
4	1.871	0.204
5	1.873	0.109

less pronounced feature within the overall imperfection field (it was predicted in four out of the five times the inverse solution was obtained for this particular case). This ability of detecting subtler features within the initial imperfection field is another useful observation to make in support of inverse solution robustness. Additionally, it is interesting to note that the favorable predictions regarding shell ultimate capacity were gleaned from single points in the load-deformation space of the problems considered.

## 2.5 Conclusions

Many diverse types of shell structures fall under the classification of being *imperfection sensitive*: meaning that the presence of even slight initial geometric imperfections result in significant erosions of predicted buckling strengths. This

behavior has important practical implications, as shell structures are applied widely in fields such as aerospace engineering, as well as naval and civil architecture. The ability to know the *actual* ultimate strength of a given shell structure has considerable value to the designer. Non-destructive means for determining this capacity is an ideal context for such assessment. / The present research has demonstrated that an inverse solution approach, employing nonlinear finite element analysis and using a divide and conquer type stochastic search algorithm, can identify the presence of localized denting imperfections in pinned barrel vault type shell structures. The predictions are made using sparse displacement measurements taken at safe, service loading conditions, in order to infer the existence and nature of the imperfection field present in a given shell structure instance. These inferred imperfections are subsequently used to make reasonably accurate predictions of actual shell structure strength at ultimate loading.

While the results presented herein are promising, it is not clear that the proposed method will yield similar accuracy across all shell structures, and across all imperfection types. This current work is merely a point of departure, from which additional studies may be made.

## **Acknowledgments**

The first two authors were partially supported in this work by a grant from the Office of Naval Research, Ship Systems and Engineering Research Division.

CHAPTER 3  
MODEL-BASED STRUCTURAL HEALTH MONITORING OF NAVAL  
SHIP HULLS<sup>1</sup>

**Abstract**

The present paper reports on results from an ongoing research program at Cornell University aimed at employing model-based structural health monitoring techniques within new and existing naval hull structures. The techniques discussed involve the solution of inverse problems, formulated using both optimization-based and Bayesian approaches. The forward modeling capability is handled using a specially developed hull structural analysis tool, CU-BEN, while the solution of the inverse problem is handled using stochastic search methods that are part of a dedicated inverse solution algorithm “toolbox,” CU-PSST. Results from the application of these tools to problems of detecting section loss in hull plating due to corrosion, and isolating damaged framing due to an internal blast, are discussed.

**3.1 Introduction**

A recent survey of active-duty United States Naval warships (Table 3.1) reveals two potential areas of concern within the U.S. Naval fleet: the average age of the fleet is between 15 and 20 years old, and the cost to replace any one ship within

---

<sup>1</sup>CHRISTOPHER J. STULL, CHRISTOPHER J. EARLS, PHAEDON-STELIOS KOUTSOURELAKIS. MODEL-BASED STRUCTURAL HEALTH MONITORING OF NAVAL SHIP HULLS. SUBMITTED TO *COMPUTER METHODS IN APPLIED MECHANICS AND ENGINEERING* ON MARCH 3, 2010

the fleet is considerable.

Table 3.1: Data from active duty naval warships [18]

Type	Aircraft Carrier	Cruiser	Destroyer	Frigate
Class	Nimitz	Ticonderoga	Burke Burke	Oliver Hazard Perry
# In-Service	10	22	53	30
Average Age (yr)	19	19	10	25
Approx. Cost (M)	\$2430	\$430	\$390	\$150

An additional, more pressing concern emanates from the ever-evolving conditions within which the fleet operates: these ship designs were conceived of some 20 to 30 years ago, and are being employed in the arena of *modern-day* naval warfare. Given the expected service lives of these vessels, such an outcome was not unforeseen, but the capabilities of these aged ship designs to meet new mission imperatives remains uncertain. In contrast to this concern, there also exists a certain level of apprehension within the naval community regarding the capabilities of *new* ship designs (*e.g.* the Freedom- and Independence-class littoral combat ships). While these radically new designs reflect significant advances in our understanding of naval hull technologies, they lack the assurances which accompany the “*tried and true*” design methodologies of the twentieth century.

Analogies may be drawn between these concerns, and those felt within the civil and aerospace engineering communities during the late 1970s and early 1980s. Such concerns subsequently gave rise to the field of structural health monitoring (SHM), and since that time, SHM has received much attention in the research community, especially during the past decade [36, 91]. While it is that Lindemann, Odland, and Strengehagen published work in 1978 related to

implementing a general hull monitoring system [66], the technology necessary for such an application was still in its infancy. Moving forward thirty years, advances in computational and sensing technologies have made more feasible, research efforts focused on *hull structural health monitoring* (HSHM), thus allowing for the vision of those early researchers to be realized. Following is a brief background of this earlier related work.

### 3.1.1 Background

Farrar, Doebling, and Nix [34] describe SHM by way of a “statistical pattern recognition paradigm,” the final step of which may be broken down into four levels [84], progressively increasing in the depth of information required:

- Step 1: Operational Evaluation;
- Step 2: Data Acquisition, Normalization and Cleansing;
- Step 3: Feature Selection and Information Condensation;
- Step 4: Statistical Model Development for Feature Discrimination:
  - Level 1: Detection;
  - Level 2: Localization;
  - Level 3: Characterization;
  - Level 4: Prediction.

This is indeed the paradigm adopted by many within the HSHM community, and for the purposes of this paper, attention is focused on a breakdown of Step 4, as it relates to ship structural systems. However, despite focusing on only one

step of this paradigm, the problem of HSHM remains a difficult one to solve: Farrar *et al.* [35] point toward the size and complexity of ship structural systems as a major hindrance. As a result of this difficulty, much of the early research related to HSHM has focused on critical components of ship structural systems rather than on the system as a whole.

Zubaydi, Haddara, and Swamidas [103], for example, employed autocorrelation functions to examine the response of stiffened plates, intended to simulate the “side shells” of ship hulls. Good agreement was shown between both the experimentally and analytically derived autocorrelation functions, demonstrating the potential promise for this method to detect, but not locate, crack damage in ship hulls. In 2002, these same authors employed neural networks, together with the finite element models developed in [103], to not only detect the presence of, but also the location and extent of various crack damage scenarios [104]. Similarly, Budipriyanto, Swamidas, and Haddara [15] developed experimental and analytical models of cross-stiffened plate structures (typical to the hulls of oil tankers) in order to determine the optimal sensor layout for measuring the dynamic response of structures, having undergone various crack damage scenarios. Using this knowledge, the authors developed a damage indicator based on the root mean square of the dynamic response amplitude. This damage indicator was capable of locating and assessing crack damage within the structure, and was subsequently built upon by the same authors in [14].

Non-traditional ship-building materials (*e.g.* composites or aluminum) have also received attention within the HSHM literature. Herszberg *et al.* [51], for example, embedded fibre Bragg grating (FBG) [96] sensors within the T-joints of glass-fibre reinforced polymer (GFRP) composite ship hulls to monitor changes

in local strain distributions (regarded as an indication of damage). Additionally, the vibrational response of these joints was examined. While both response measures (*i.e.* strains and vibrations) showed promise in the detection of damage, the authors stated that the *assessment* of this damage was “far from trivial and will require considerable research effort.” Building on this work, Li *et al.* [64] implemented a HSHM system capable of both detecting *and* assessing damage within T-joints of GFRP ship hulls. In addition to embedded FBG sensors, a statistical outlier analysis of the resulting sensor data was implemented in order to distinguish *states of damage* within T-joints. More recently, Silva-Muñoz and Lopez-Anido [88] proposed a method of detecting crack propagation in composite joints by correlating it with changes in local strain distributions obtained using embedded FBG sensors.

As mentioned previously, the complexity associated with ship structural systems has been the primary hurdle in the development of *full-scale* HSHM systems. Indeed, until recently, the literature related to full-scale HSHM systems has primarily involved a system developed by the Norwegian Defense Research Establishment [97]<sup>2</sup>. Similar to [51, 64, 88], the primary components of the HSHM system are FBG sensors embedded within the composite hull. However, in addition to monitoring “locations critical to the ship design,” the sensor layout was constructed such that the structural health of the *overall* system could also be monitored. Preliminary results of this ongoing work (primarily based on sea-trials) have shown promise, and implementation of the system in additional ships is currently underway. More recently, full-scale HSHM research efforts have focused on the all-aluminum hulls of littoral combat ships [85, 70], with

---

<sup>2</sup>This system is a culmination of the work related to the “Composite Hull Embedded Sensor System” (CHESS) project initiated in 1996 as a joint research effort between the United States Naval Research Laboratory and Norwegian Defense Research Establishment (see [98], and references contained therein).

the latter reference focusing more on the instrumentation aspect of the problem.

Now, despite the stochastic nature of the environments in which naval vessels typically operate, efforts at addressing the inherent *uncertainty* within HSHM predictions are somewhat lacking in the literature. At a recent conference session on SHM for ship structures, Nichols *et al.* [74] introduced the use of Bayesian statistical inference, by way of a Markov Chain Monte Carlo algorithm, as a means of inferring damage from experimental data. However, while research efforts in the civil engineering community have adopted similar strategies to address this concern (see *e.g.* [102, 17, 75]), to the authors' knowledge, efforts at applying such strategies directly to ship structural systems remains unseen.

Taking this as a point of departure, the present paper is aimed at the development and application of SHM techniques to full-scale ship structural systems. In contrast to the above references (sans [74]), a *model-based* paradigm is adopted, employing two distinct approaches to solve the resulting HSHM problem: a classical approach and, to more formally address the issue of uncertainty in the predictions, a probabilistic approach which adopts a Bayesian framework. As a means of testing these approaches, two representative damage scenarios are proposed and solved within the confines of a hypothetical, idealized hull structural system.

### **3.1.2 Paper organization**

Formulations of the forward and inverse problems associated with this research are provided in Section 3.2. Section 3.3 provides a description of the two demon-

stration problems examined in this work, as well as details on the stochastic search algorithms employed to solve these problems. Results are presented in Section 3.4, with a discussion of the relevant details included; conclusions drawn from these results are then provided in Section 3.5.

## 3.2 Formulation

The present research adopts a model-based paradigm in its approach to HSHM. The goals of model-based HSHM are no different from those of the examples presented in Section 3.1.1 (*i.e.* to detect, locate, and characterize damage within ship structural systems); the difference arises from the approach to the problem. Whereas traditional SHM methods pursue these goals by comparing observed response data against previously established statistical models, in an attempt to detect statistical anomalies (*i.e.* damage), the goal of model-based SHM is to infer an analytical model directly from the observed response data. This is traditionally posed as the following inverse problem [39]: “Given some observed response from a potentially damaged structural system, due to some external action, determine an analytical model of the structural system which accurately captures this observed response.” The successful discovery of this analytical model then provides *direct* insight into the physical condition of the system, effectively completing Levels 1 through 3 (from Step 4 of the statistical pattern recognition paradigm outlined previously). Moving forward, this analytical model may also be employed to examine myriad “virtual proof testing scenarios,” extending the approach to meet a new objective: *prognosis*.

Model-based SHM approaches are often broken into two parts: the forward

problem and the inverse problem: with the results of the latter depending upon the former. Formal descriptions of each, within the context of the present paper, are presented in the following two sections.

### 3.2.1 Forward problem

In its most general form, the forward problem comprises a linear system, described by the following partial differential equation (PDE):

$$\mathcal{A}(f(\mathbf{x}; \Theta)) u(\mathbf{x}) - b(\mathbf{x}) = 0 : \mathbf{x} \in \Omega \subset \mathbb{R}^3, f(\mathbf{x}; \Theta) \in \mathbf{F} \quad (3.1)$$

where the above terms are defined as follows:

$\mathcal{A}(f(\mathbf{x}; \Theta))$  is a linear differential operator describing the system, characterized by  $f(\mathbf{x}; \Theta)$ ,

$\mathbf{x}$  is a spatial coordinate within the domain of the system,  $\Omega$ , which is itself a subset of  $\mathbb{R}^3$ ,

$\Theta$  is a set of parameters which describe the damage (see Section 3.2.3),

$\mathbf{F}$  is the collection of all possible damaged characterizations of the system, and

$u(\mathbf{x})$  is the response of the system, due to some external action,  $b(\mathbf{x})$ .

Employing the finite element method, the PDE given in Equation (3.1) may be discretized into a linear system of equations as,  $\mathbf{A}\mathbf{u} = \mathbf{b}$  (note that the dependency of  $\mathbf{A}$  on  $f(\mathbf{x}; \Theta)$  has been removed to simplify the notation). Obtaining the response vector,  $\mathbf{u}$ , is thus achieved by pre-multiplying the load vector,  $\mathbf{b}$ , by the inverse of the system matrix,  $\mathbf{A}$ .

As it is that inverse solution strategies typically require numerous calls to the forward solver, the time necessary to arrive at the solution to a given inverse problem is almost entirely driven by the time required of the forward solutions. It is therefore important, when developing such inverse solution strategies that the efficiency of the forward solver be a concern. It is for this reason that efforts were focused by the authors on the development of a fully nonlinear finite element code, CU-BEN (it is noted that for the present paper, the example problems are executed in the linear-elastic regime). Written in ANSI C99 and employing the MPI standard, the current version of CU-BEN employs an updated Lagrangian reference frame with three structural element formulations: a 6-degree-of-freedom (DOF) truss [4], a 14-DOF frame [72], and an 18-DOF triangular shell [10, 8, 9]. While these elements have been shown to effectively predict geometrically nonlinear behavior, they were primarily chosen due to the efficient treatment of material nonlinearity through a force-space plasticity approach [72, 21, 22], which precludes the need for expensive integrations through the elements' cross-sections. With the additional ability to incorporate member end offsets and / or releases into the frame elements, models developed using CU-BEN are capable of accurately capturing many of the salient features present in ship structural systems, while still serving as an efficient forward solver in support of the inverse solution.

### **3.2.2 Inverse problem**

We begin our discussion of the inverse problem in a general context, by first assuming the presence of a sparse, distributed sensor array which measures the response of the ship structural system under assumed service conditions. This

collection of *observed* responses is given as:

$$\mathbf{U}_{\text{obs}} = \{u_{\text{obs}}(\mathbf{x}) : \mathbf{x} \in \Omega \subset \mathbb{R}^3\} \quad (3.2)$$

The solution of the forward problem discussed in the previous section produces an analogous collection of *model* responses, given as:

$$\mathbf{U}_{\text{FE}}(f(\mathbf{x}; \Theta)) = \{u_{\text{FE}}(\mathbf{x}; f(\mathbf{x}, \Theta)) : \mathbf{x} \in \Omega \subset \mathbb{R}^3, f(\mathbf{x}; \Theta) \in \mathbf{F}\} \quad (3.3)$$

Having defined these quantities, the solution of the inverse problem is aimed at obtaining information about the parametric representation of the ship structural system,  $f(\mathbf{x}; \Theta)$ , as it relates to the observed data,  $\mathbf{U}_{\text{obs}}$ . The commonly adopted, or so-called “classical approach” to solving such problems is to cast them in the form of a functional optimization as:

$$\min_{\Theta} J(f(\mathbf{x}; \Theta)) \quad (3.4)$$

where  $J(f(\mathbf{x}; \Theta))$  is an objective functional, given as:

$$J(f(\mathbf{x}; \Theta)) = \|\mathbf{U}_{\text{obs}} - \mathbf{U}_{\text{FE}}(f(\mathbf{x}; \Theta))\| \quad (3.5)$$

and  $\|\cdot\|$  represents any appropriate norm, comparing  $\mathbf{U}_{\text{obs}}$  and  $\mathbf{U}_{\text{FE}}(f(\mathbf{x}; \Theta))$ . The subsequent solution of Equation (3.4) provides the desired analytical model, characterized by  $f(\mathbf{x}; \Theta)$ , which most closely produces the observed responses.

This is indeed one of the approaches adopted for the research reported upon herein; specific details related to this classical approach are presented in Section 3.3.3. The other adopted approach employs techniques from Bayesian inference to cast the above within a probabilistic context. A brief background concerning this latter approach is provided in the following section, prior to the introduction of the example problems in Section 3.3.

## Bayesian formulation

Bayesian formulations represent a stochastic counterpart of classical (*i.e.* optimization-based) solution methods. Adopting this approach, the unknown model parameters,  $\Theta$ , are considered to be random variables, with the inference process aimed at obtaining posterior probability distributions on these unknowns. Such distributions then allow the analyst to quantify the relative plausibilities of various values of the model parameters,  $\Theta$ . Bayesian formulations offer several advantages to the analyst, as they provide a unified framework for dealing with the uncertainty introduced by incomplete and noisy measurements, as well as quantitatively assessing the resulting inferential uncertainties. Significant successes using this approach have been noted in applications such as medical tomography [101], geological tomography [44, 2], hydrology [63], petroleum engineering [50, 20], as well as a host of other physical, biological, and social systems [59, 87, 99, 67].

One of the basic elements of Bayesian models is the *likelihood* function,  $L(\Theta) = p(\mathbf{U}_{\text{obs}} | f(\mathbf{x}; \Theta))$ .  $L(\Theta)$  is a conditional probability distribution which gives a relative measure of the propensity of observing data,  $\mathbf{U}_{\text{obs}}$ , for a given model configuration specified by  $f(\mathbf{x}; \Theta)$ . The likelihood function is also encountered in frequentist formulations where the unknown model parameters are determined by maximizing  $L(\Theta)$ . The second component of Bayesian models is the *prior* distribution,  $p(\Theta)$ , which encapsulates in a probabilistic manner, any knowledge / information / insight that is available to the analyst prior to observing the data. The combination of the *likelihood* function and the *prior* distribution, based on Bayes' rule, yields the *posterior* distribution,  $\pi(\Theta)$ , which probabilistically summarizes the information extracted from the data, with re-

gard to the unknown model parameters:

$$\underbrace{\pi(\Theta)}_{\text{posterior}} = p(\Theta | \mathbf{U}_{\text{obs}}) \propto \underbrace{p(\mathbf{U}_{\text{obs}} | f(\mathbf{x}; \Theta))}_{\text{likelihood}} \underbrace{p(\Theta)}_{\text{prior}} \quad (3.6)$$

Although the prior is a point of frequent criticism due to its inherently subjective nature, it can prove extremely useful in engineering contexts, as it provides a mathematically consistent vehicle for injecting the analyst’s insight and physical understanding into the inference process. More importantly perhaps, it can readily be shown that regularization terms (*e.g.* Tikhonov regularization [95]) that are frequently used in classical formulations amount to the adoption of specific priors. For example, the absence of a regularization term in Equation (3.5) corresponds to a uniform prior. In this study, *hierarchical* prior models are adopted. These prior models, described in Section 3.2.3, both subdue the effects of prior specifications in the final inference results and promote sparsity in the solution.

Representations of the parametric fields in existing approaches artificially impose a minimum length scale of variability, usually determined by the discretization size of the governing PDEs [63]. Furthermore, these fields are typically associated with a very large vector of unknowns. Inference in high-dimensional spaces using standard Markov Chain Monte Carlo (MCMC) schemes, which for years have served as the workhorses of Bayesian computation, is generally impractical as it requires an exuberant number of calls to the forward solver in order to achieve convergence. Care must be taken, therefore, in choosing an appropriate scheme to arrive at the solutions of the posterior distributions given in Equation (3.6). Details of the techniques employed for the present research are provided in Section 3.3.3.

### 3.2.3 Parameterization of damage

Having provided general descriptions of the forward and inverse problems, it is now appropriate to focus attention on the definition of  $f(\mathbf{x}; \Theta)$  which provides the mechanism by which damage may be inserted into the system. Consider, for example, an explicit representation of shell element thicknesses, in which the original shell element thicknesses are potentially reduced to model the effects of corrosion:

$$f(\mathbf{x}; \Theta) = t_i \leq (t_o)_i \quad (3.7)$$

where  $i = 1, 2, \dots$ , number of elements in a hull model.

While this represents a valid means of inserting damage into the system, such an approach presents difficulties with respect to the solution of the inverse problem, as the solution would depend on a parameter set of size equal to the number of elements within the finite element model (see Section 3.2.2). In this spirit,  $f$  is characterized by a set of parameters,  $\Theta$ , where the intent of these parameters is to incorporate *a priori* knowledge about the damage being considered, using a reduced basis. For the above example, it would be realistic to, instead of considering individual elements, consider *sets* of elements, thereby reducing the dimensionality (*i.e.* number of sets vs. number of elements), while maintaining a realistic representation of the damage (*i.e.* that corrosion occurs within reasonably sized regions).

Specific to the example problems considered in the present paper, a physically meaningful way to model damage is through a reduction of section properties. This translates to: a reduction in shell thicknesses for the corrosion problem and a reduction in the frame member depths for the framing damage problem (which in turn, affects related section properties). Taking into account that both

of these damage types are typically confined to specific regions within the hull, a convenient and natural means of parameterizing the damage is to employ Gaussian radial basis functions (RBFs) [48] as follows. We first denote the collection of section properties of interest (*e.g.* shell thicknesses) by  $\Gamma$ , with an analogous collection of initial, undamaged section properties denoted by  $\Gamma_o$ . Reduction of these section properties may now be achieved by applying the following equation:

$$\Gamma \approx \Gamma_o - \sum_{i=1}^N \omega_i \Psi_i(\mathbf{x}) \quad (3.8)$$

where  $N$  is the number of Gaussian RBFs used in the approximation of the damaged configuration and  $\omega_i$  are Fourier coefficients representing the maximum reduction in the section properties.  $\Psi_i(\mathbf{x})$  then represents a Gaussian RBF given by:

$$\Psi_i(\mathbf{x}) = \exp\left(-\left(\frac{\|\mathbf{c}_i - \mathbf{x}\|_{\ell^2}}{\sqrt{2}\tau_i}\right)^2\right) \quad (3.9)$$

where  $\mathbf{c}_i$  are the *two-dimensional* RBF centers and  $\tau_i$  are their standard deviations. The reduction in the dimensional representation of the RBF centers is achieved through a previous transformation of the hull side shells in which a hypothetical and highly idealized V-shaped hull is effectively “fileted” by rotating the hull side shells, about the longitudinal keel line, until they lie in a coincident coordinate plane (see Figure 3.1).

$\Theta$  may now be given as the following collection of damage model parameters:

$$\Theta = \left[ \omega_1 \quad \mathbf{c}_1 \quad \tau_1 \quad \cdots \quad \omega_N \quad \mathbf{c}_N \quad \tau_N \right]^T \quad (3.10)$$

where, as above,  $N$  is the number of Gaussian RBFs used in the approximation of the damaged configuration. Additionally, while  $N$  may be fixed at a single value, the authors chose to leave it as an unknown. It is therefore important to note that  $N$  is *also* regarded as a model parameter when considering

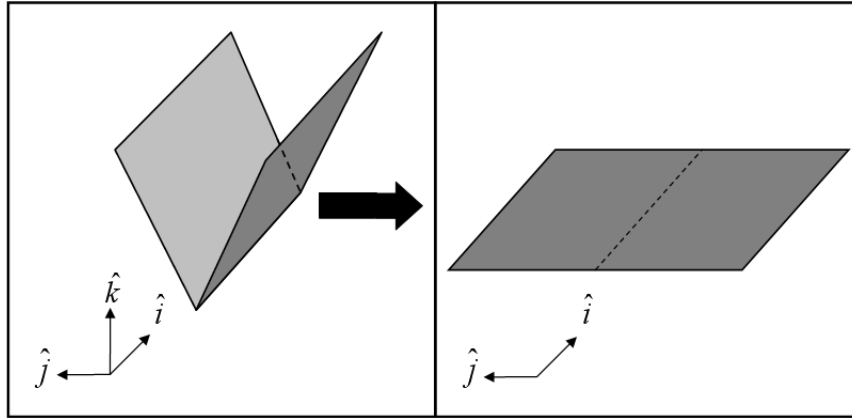


Figure 3.1: Transformation of hull side shells into a two-dimensional representation

the stochastic search approaches and example problems presented herein. This parameterized damage model, while providing a reduced basis from which the solution may be drawn, also affords a certain amount of flexibility, as the number of RBFs employed essentially dictates the resolution to which the actual damage may be approximated. For example, fewer RBFs may be unable to effectively capture the fine-scale details of more complex damage scenarios, but could quickly provide a coarse approximation of the damage, by searching over a reduced number of parameters. The converse is also true: many RBFs, with a correspondingly large number of parameters, while able to capture fine-scale details, would in turn increase the time required to arrive at a solution. Such flexibility naturally lends itself to a multi-scale approach to the solution of the inverse problem, a problem which the authors hope to address in future research efforts.

## Prior and likelihood specification

The most critical component in constructing Bayesian models involves the prior specification for the unknown material properties, represented by  $f(\mathbf{x}; \Theta)$ . In existing Bayesian [99] as well as classical formulations,  $f(x)$  is discretized according to the spatial resolution of the forward solver. For example, in cases where finite elements are used, the property of interest is assumed to be constant within each element, and therefore the vector of unknowns is of dimension equal to the number of elements. This offers obvious implementation advantages but also poses some difficulties since the scale of variability of material properties is implicitly selected by the solver rather than the data. This is problematic in several ways. On one hand, if the scale of variability is larger than the grid, a waste of resources takes place, at both the solver level, which has to be run at unnecessarily fine resolutions, and at the level of the inference process, which is impeded by the unnecessarily large dimension of the vector of unknowns. Furthermore, as the number of unknowns is much larger by comparison to the amount of data, it can lead to *over-fitting*. This will produce erroneous values for the unknowns that may nevertheless fit the data perfectly. Such solutions will have negligible *predictive ability* and would thus be useless in decision-making processes. On the other hand, if the scale of variability is smaller than the grid, the unknown material properties cannot be identified, even if the solver provides sufficient information for discovering this possibility.

An important addition to the vector of model parameters given in Equation (3.10), is the number of terms,  $N$ , in the expansion of Equation (3.8). Hence the *cardinality* of the model (*i.e.* the number of RBFs) is the key unknown that must be determined so as to provide a good interpretation of the observables.

Independently of the form of the kernel adopted, the important, common characteristic of all such approximations is that the field representation does not depend on the resolution of the forward model. The latter affects inference only through the “black-box” functions given in Equation (3.3). A summarized version of the prior models adopted in this work is provided below. A detailed justification can be found in [60].

- $N$ : the number of kernel functions. We employ a Poisson distribution,  $p(N | \lambda) = \frac{\lambda^N}{N!} \exp(-\lambda)$ , with an exponential hyperprior for the hyperparameter,  $\lambda$ .
- $\{\omega_i\}_{i=1}^N$ : the coefficients of the expansion in Equation (3.8). A multivariate normal,  $N(\mathbf{0}, \sigma_a^2 \mathbf{I})$ , is used and a Gamma hyperprior for the hyperparameter,  $\sigma_a^2 \sim \text{Gamma}(a_0, b_0)$ .
- $\{\tau_i^{-1}\}_{i=1}^k$ : the precision parameters of each kernel which pertain to the scale of the unknown field(s). We employ independent Gamma priors:

$$p(\{\tau_i^{-1}\}_{i=1}^N | N, a_\tau, b_\tau) = \prod_{i=1}^N \frac{b_\tau^{a_\tau}}{\Gamma(a_\tau)} \tau_i^{-a_\tau+1} \exp\left(-\frac{b_\tau}{\tau_i}\right) \quad (3.11)$$

In order to automatically determine the mean of the Gamma prior, we express  $b_\tau = \mu_i a_\tau$ , where  $\mu_i$  is a location parameter for which an exponential hyperprior is used with a hyperparameter,  $a_\mu$ .

- $\{c_i\}_{i=1}^N$ : the locations of the kernels which are points in  $\mathbf{\Omega}$  for which a uniform distribution in  $\mathbf{\Omega}$  is used.

The observed output,  $u_{\text{obs}}(\mathbf{x})$ , at  $n$  locations within  $\mathbf{x} \in \mathbf{\Omega}$  is assumed to be related to the model predictions,  $u_{\text{FE}}(\mathbf{x}; f(\mathbf{x}; \Theta))$ , as follows:

$$u_{\text{obs}}(\mathbf{x}) = u_{\text{FE}}(\mathbf{x}; f(\mathbf{x}; \Theta)) + e(\mathbf{x}) \quad (3.12)$$

where  $e(\mathbf{x})$  quantify the deviation between model predictions and data. The probabilistic model for  $e(\mathbf{x})$  in Equation (3.12) gives rise to the *likelihood* function,  $L(\Theta)$ . In the simplest case, where  $e(\mathbf{x})$  are assumed independent, normal variates with zero mean and variance,  $\sigma_e^2$  (note that the functional dependencies have been removed from  $u_{\text{obs}}$  and  $u_{\text{FE}}$  to simplify the following notation):

$$p(u_{\text{obs}} | \Theta, \sigma_e) \propto \frac{1}{\sigma_e} \exp\left(-\frac{1}{2} \frac{(u_{\text{obs}} - u_{\text{FE}})^2}{\sigma_e^2}\right) \quad (3.13)$$

and

$$\begin{aligned} L(\Theta) &= p(\mathbf{U}_{\text{obs}} | \Theta, \sigma_e) \\ &= \frac{1}{\sigma_e^n} \exp\left(-\frac{1}{2\sigma_e^2} \sum_{\mathbf{x}} (u_{\text{obs}} - u_{\text{FE}})^2\right) \end{aligned} \quad (3.14)$$

More complex models which can account for the spatial dependence of the error variance or the detection of events associated with sensor malfunctions at certain locations, can readily be formulated. In general, the variances,  $\sigma_e^2$ , are unknown (particularly, the component that pertains to model error) and should be inferred from the data. When a conjugate, *Gamma*( $a, b$ ) prior is adopted for  $\sigma_e^{-2}$ , the error variances can be integrated out from Equation (3.13), further simplifying the likelihood:

$$L(\Theta) \propto \frac{\Gamma(a + n/2)}{\left(b + \frac{1}{2} \sum_{\mathbf{x}} (u_{\text{obs}} - u_{\text{FE}})^2\right)^{a+n/2}} \quad (3.15)$$

where  $\Gamma(z) = \int_0^{+\infty} t^{z-1} e^{-t} dt$  is the Gamma function.

The complete model is now summarized as follows. Let  $\Theta_N = \{\{\omega_i\}_{i=1}^N, \{\tau_i^{-1}\}_{i=1}^N, \{\mathbf{c}_i\}_{i=1}^N\}$  denote the vector containing all the unknown parameters and  $\Theta = (N, \Theta_N)$ . Since  $N$  is also assumed unknown and allowed to vary, the dimension of  $\Theta_N$  is variable as well. In two-dimensional problems for example the dimension of  $\Theta_N$  is  $(N + 1) + N + 2N = 2 + 4N$ . Based on the aforementioned

equations, the complete prior model is given by:

$$\begin{aligned}
p(\Theta | s, a_\tau, a_\mu, a_0, b_0) &= \frac{1}{(s+1)^{N+1}} \\
&\times \prod_{j=1}^N \frac{\Gamma(a_\tau + 1)}{\Gamma(a_\tau)} \frac{a_\tau^{a_\tau}}{\tau_i^{-(a_\tau-1)}} \frac{1}{a_\mu} \frac{1}{\left(\frac{a_\tau}{\tau_i} + a_\mu^{-1}\right)^{(a_\tau+1)}} \\
&\times \frac{1}{(2\pi)^{N/2}} \frac{\Gamma\left(a_0 + \frac{N}{2}\right)}{\left(b_0 + \frac{1}{2} \sum_{j=1}^N a_j^2\right)^{a_0+N/2}} \times \frac{1}{|\mathbf{\Omega}|^N}
\end{aligned} \tag{3.16}$$

### 3.3 Example problems

Two example problems are presented to demonstrate the techniques outlined in Section 3.2. The first problem, “Example Problem 1,” examines the issue of detecting corrosion within a hypothetical ship structural system, while the second problem, “Example Problem 2,” examines the issue of detecting internal blast damage within frame members which act to stiffen the side shells of a hypothetical hull. Each of these problems is solved employing both the functional optimization framework outlined in Section 3.2.2, and through the Bayesian inference framework outlined in Section 3.2.2.

As is it that the use of actual, or even representative, hull geometries is a sensitive issue when considering survivability and post-event performance of naval vessels, the current discussion centers on a highly idealized hypothetical hull geometry (see Figure 3.2). While the selected lines and scantlings (*i.e.* overall geometry and member dimensions) are in no way representative of a practical design, they are in fact consistent with a common class of naval vessels in use throughout the world’s navies.

The overall dimensions of the hypothetical hull structure are: length from

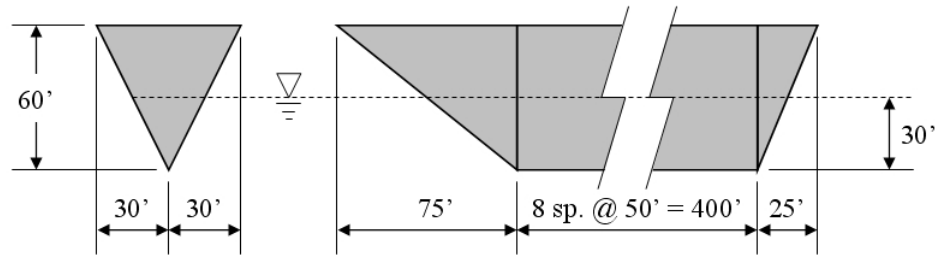


Figure 3.2: Gross dimensions of idealized ship structural system

bow to stern of 152.39 m (500'), beam (*i.e.* width at "top deck" from port to starboard) of 18.29 m (60'), and height from keel to "top deck" of 18.29 m (60'). There also exist nine transverse bulkheads, located at 15.24 m (50') intervals throughout the ship, resulting in 8 compartments (the bow and stern sections are 22.86 m (75') and 7.62 m (25') long, respectively). All components of the hull are modeled using triangular shells [10, 8, 9] with nodal spacing at approximately 1.52 m (5') intervals. To model the case of a ship moored at port, pinned boundary conditions are applied along the keel with vertical rollers imposed along all top, exterior edges composing the "top deck." Hydrostatic loading conditions are applied to all nodes which fall below the waterline, where the draft of this hypothetical ship is approximated 9.14 m (30') (see Figure 3.2). While the above description holds for both problems examined in the current work, two distinct finite element models are employed for each problem.

### 3.3.1 Example Problem 1

The extreme environments in which ocean going vessels operate, together with their typically long service lives, result in a situation where the potential for a reduction in hull plating due to corrosion is a significant concern. The exterior

hull side shell thicknesses are one focus of the present research, and a finite element model, built in CU-BEN, is employed to model this case. The model incorporates 20.32 cm (8") thick exterior plating with 2.54 cm (1") thick transverse bulkheads (see Figure 3.3). The reduction in thickness of the hull side shells is subsequently modeled on an element-by-element basis, where the  $x$  employed in Equations (3.8) and (3.9), are the centroids of the triangular shells.

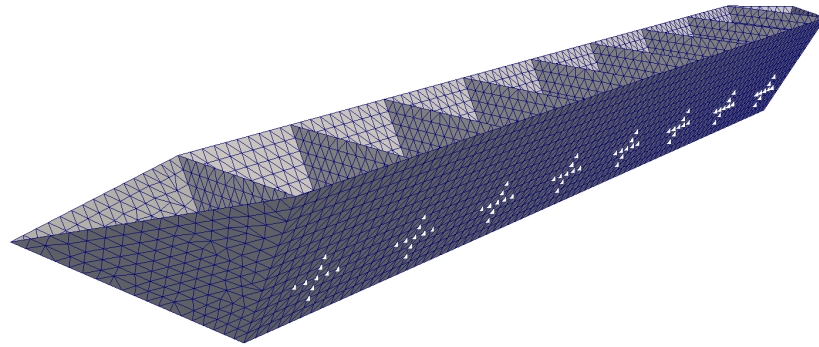


Figure 3.3: Schematic of finite element mesh for Example Problem 1 displaying data sampling configuration (white triangles)

Also given in Figure 3.3 is the data sampling configuration employed for this problem; an analogous configuration is also present on the starboard side. A sensitivity study, in which parameters of the damage model were varied over their respective ranges, yielded points clustered around the white "criss-cross" patterns, as those exhibiting the greatest variance between observed regions. Subsequently, a criss-cross pattern was proposed for each of the eight compartments, resulting in 144 total data points. While this pattern is intuitive, with respect to the hydrostatic loading conditions present within the model, and proved capable of capturing the desired response, such a data sampling configuration is far less capable of detecting damage *above* the waterline; this is an acceptable result, given that corrosion is less likely to occur above the waterline.

### 3.3.2 Example Problem 2

Internal blast damage in the ship structural system is defined as a reduction in the cross-sectional characteristics of the frame members that stiffen the side shells of the hull. Such damage may arise from weapon system malfunctions, resulting in internal explosions within the ship. Identification of this type of damage highlights the potential of the HSHM system to provide prognoses of future performance: a very real concern for naval vessels damaged at sea. Finally, it is noted that internal explosions which cause a breach of the exterior hull plating are not being considered in the present study.

Figure 3.4 presents a schematic of the structural framing, modeled through multiple lattices of rectangular frame elements within each compartment, where the shell finite element mesh is omitted for clarity. Both the exterior hull plating thickness and the transverse bulkheads are set at 2.54 cm (1"). As in Example Problem 1, Equations (3.8) and (3.9) are employed to reduce the depths of the frame elements (initially set at 60.96 cm (24")), and  $\mathbf{x}$  are the centroids of these frame elements; cross-sectional characteristics are then computed using these reduced depths.

The procedure employed to arrive at the data sampling configuration given in Figure 3.4 is identical to that outlined for Example Problem 1. In this case, however, it was discovered that intersections of the frame elements proved to be most sensitive to the varying of the damage model parameters, resulting in a total of 192 data points. As observed formerly, the restriction regarding the detection of damage above the waterline is present in this problem.

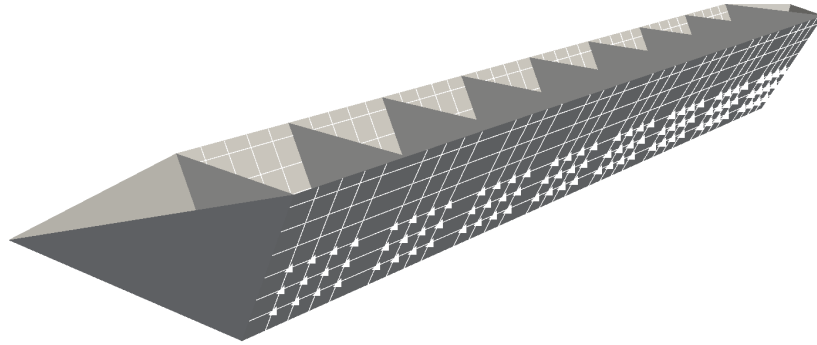


Figure 3.4: Schematic of finite element mesh for Example Problem 2 displaying data sampling configuration (white triangles)

### 3.3.3 Stochastic search approaches

Section 3.2 outlines two formulations of the model-based HSHM problem: one adopting a functional optimization framework and one adopting a Bayesian statistical inference framework. While the overarching goal of these two formulations is to gain insight into the health of ship structural systems, both the solutions and the methodologies employed to arrive at these solutions, differ significantly.

#### Genetic algorithm for functional optimization

The functional optimization algorithm chosen for the present work is a genetic algorithm (GA) [46, 73, 68, 49]. GAs adopt a “survival-of-the-fittest” approach to the problem of functional optimization, wherein individuals composing a population “compete” for survival according to their fitness level. Individuals with desirable traits, reflected through their fitness, are carried forward from one generation to the next, while those with less desirable traits are removed

from the population through various selection pressures. Within the context of the present paper, an individual is regarded as a configuration of the ship structural system, represented by the model parameters given in Equation (3.10). In addition to adopting a rather intuitive solution scheme, GAs are also well-suited to problems which exhibit complicated objective functional(s): a common issue when dealing with model-based SHM formulations [93]. Such objective functionals are often of a non-convex nature [68], thus eliminating the more efficient gradient-based solvers from consideration, due to their inability to negotiate solution spaces containing multiple local minima [16, 81].

While numerous variants of the GA have been proposed and successfully demonstrated on a variety of problems (see *e.g.* [68]), most GAs involve, in one capacity or another, computational models of the following evolutionary processes: elitism, selection, crossover, and mutation<sup>3</sup>. Indeed, the present research adopts these basic aspects of a GA, as given by the flowchart in Figure 3.5. A discussion of the details associated with each step is now presented.

Following the random initialization of the first generation, individuals within the population are evaluated through executions of the forward solver (see Section 3.2.1). This forward solution includes calculation of the objective functional value for each individual, given as the sum of the  $\ell^2$  and  $\ell^\infty$  norms as:

$$J(f(\mathbf{x}; \Theta)) = \| \mathbf{U}_{\text{obs}} - \mathbf{U}_{\text{FE}}(f(\mathbf{x}; \Theta)) \|_{\ell^2} + \| \mathbf{U}_{\text{obs}} - \mathbf{U}_{\text{FE}}(f(\mathbf{x}; \Theta)) \|_{\ell^\infty}$$

where the components of  $\mathbf{U}_{\text{obs}}$  and  $\mathbf{U}_{\text{FE}}(f(\mathbf{x}; \Theta))$  are displacements normal to the side shell of the hull taken at 144 points, in the case of Example Problem 1, or 192 points, in the case of Example Problem 2 (see Figures 3.3 and 3.4). As the

---

<sup>3</sup>A discussion of the various methods employed to model these evolutionary processes is beyond the scope of this document. The reader is directed to [46, 73, 68, 49] for more thorough discussions of methods to model these, and other such evolutionary processes.

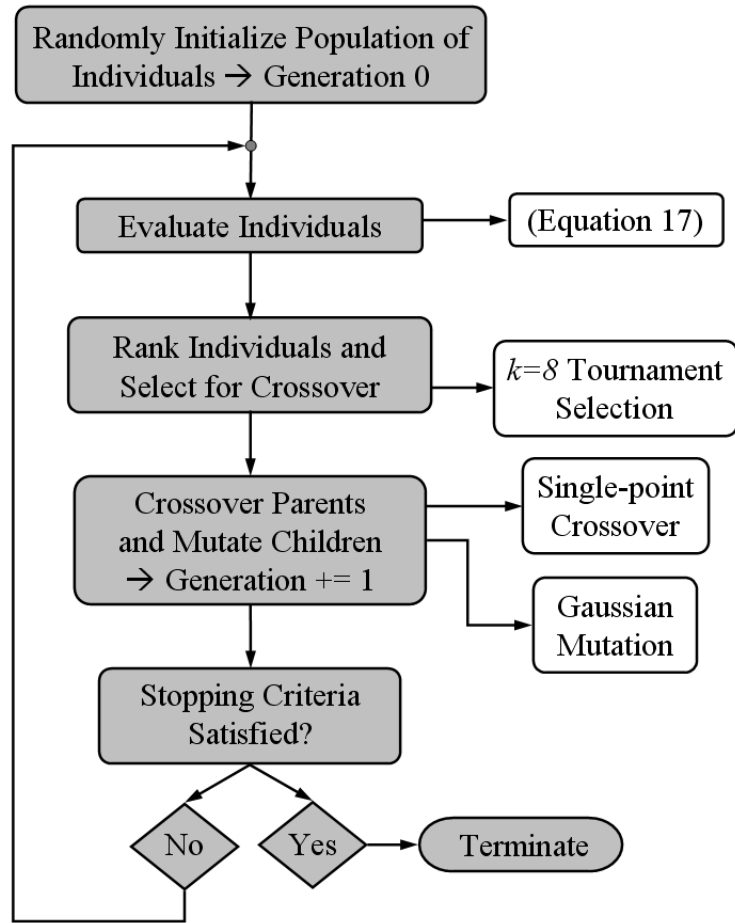


Figure 3.5: Features of the genetic algorithm employed for the paper

present examples employ analytical models of idealized ship structural systems,  $\mathbf{U}_{\text{obs}}$  constitutes *simulated* experimental data, and is thus derived from a forward solution of the analytical model incorporating the target damage scenario, with the addition of Gaussian noise at a signal-to-noise ratio of 1000. It is noted that the definitions of  $\mathbf{U}_{\text{obs}}$  and  $\mathbf{U}_{\text{FE}}(f(\mathbf{x}; \Theta))$ , as well as the noise imposed on  $\mathbf{U}_{\text{obs}}$ , hold for both the functional optimization approach as well as the Bayesian statistical inference approach treated in the sequel.

Having completed the forward evaluations, the individuals are ranked, and the individual exhibiting the minimum objective functional value is deemed the

“most fit” within the population (this individual is automatically propagated to the next generation as a result of “elitism”). With evaluation and ranking complete, so-called “parent” individuals are selected through a  $k = 8$ -tournament-based selection function. This function randomly selects  $k$  individuals from the population to compete in a tournament; the most fit individual from the subgroup wins the tournament and is selected as a parent, with the process repeating until the required number of parents is reached. Parents are then paired up and undergo the process of crossover, with a success rate of 85%; a single-point crossover function is employed in the present work (see Figure 3.6), yielding a pair of so-called “children” for each pair of parents.

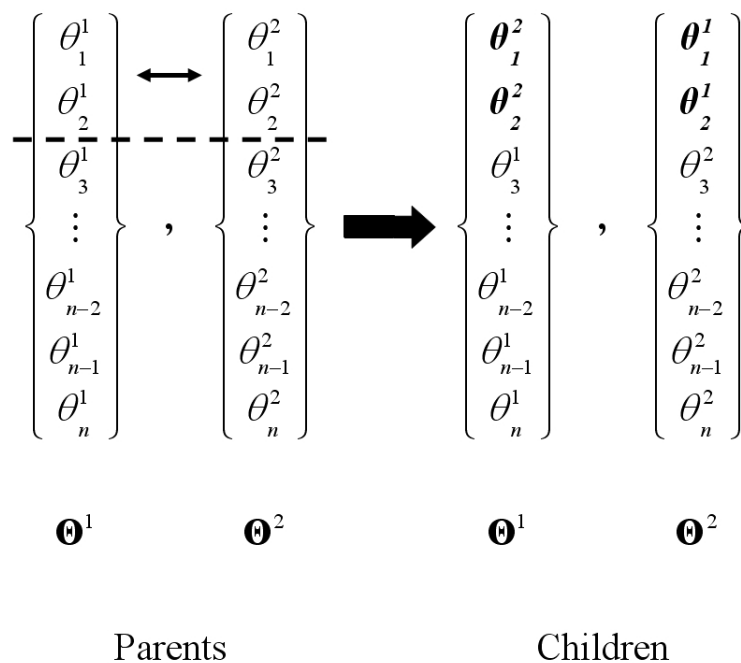


Figure 3.6: Schematic of parents undergoing single-point crossover; the dashed line represents the *random* point at which parameters are swapped

Following crossover, all parameters composing each of these children undergo mutation (a success rate of 0.75% is employed) through a Gaussian mutation function. This function is designed to mutate parameters in a Gaussian

fashion with a variance which monotonically decreases as the number of GA generations increase throughout the solution. These potentially mutated children then compose the next generation within the GA, and the process is repeated until the stopping criteria (*i.e.* a maximum number of generations) is met.

The capability of GAs to negotiate non-convex objective functionals, while advantageous, should not be overestimated, and thus efforts at improving robustness should be carefully considered. In this spirit, a “divide-and-conquer” scheme [93] is also adopted in the present work; a schematic of this process is given in Figure 3.7. The first step of this approach divides the global solution space into local solution spaces, with respect to the spatial parameters,  $c_i$ . For this step, the eight compartments formed by the transverse bulkheads are employed as bounds of the local solution spaces. Employing these spatial bounds, the GA described previously is executed eight times (once for each of the eight local solution spaces), and the resulting optimal solutions are recorded. These solutions are then employed in the construction of the initial population for a final GA execution, searching over the global solution space (*i.e.* the entire hull). In this manner, the solution is arrived at in an incremental fashion, by first solving local problems of reduced difficulty, and then employing these solutions to inform the more difficult global solution.

A summary of the above solution process is now presented, where the only difference between the example problems lies in the number of individuals composing a population; differing values for Example Problem 2 are given in parentheses. It is noted that due to the stochastic nature inherent in GAs, the solution process presented below was executed five times in order to obtain an average

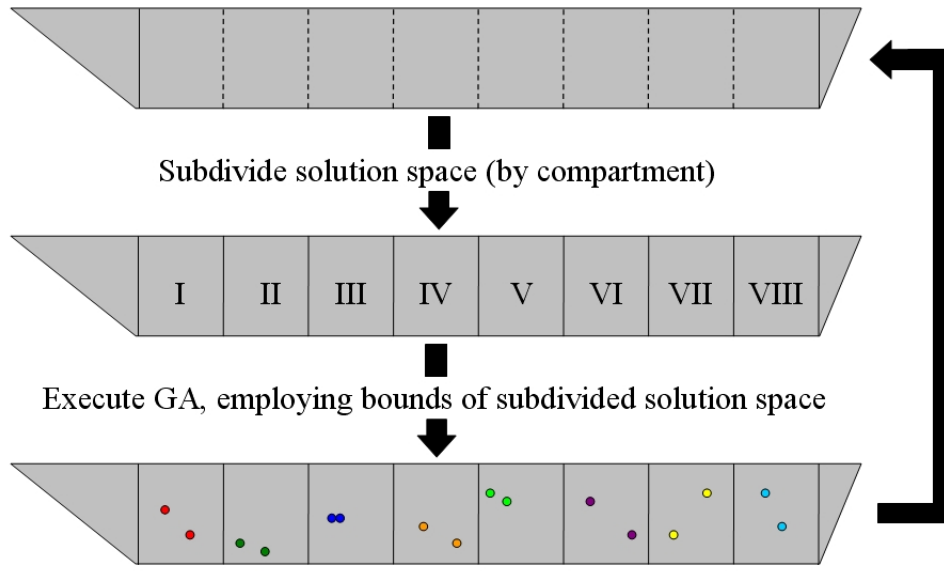


Figure 3.7: Schematic of divide-and-conquer solution scheme

“optimal” solution.

### Sequential Monte Carlo inference to determine the posterior

Shifting our focus to the Bayesian formulation of the problem, we take as our point of departure the fact that the posterior defined in Equation (3.6) is analytically intractable. For that reason, *Monte Carlo* methods are relied upon in the present work, as they are essentially the only accurate way to carry out the inference task. Traditionally (and more specifically), Markov Chain Monte Carlo techniques have been employed [52, 38]. These techniques are based on building a Markov chain that asymptotically converges to the target density (in this case, the posterior,  $\pi(\Theta)$ ) by appropriately defining a transition kernel. While convergence can be assured under weak conditions [69], the rate of convergence can be extremely slow and require a large number of likelihood evaluations and calls to the forward solver. Particularly, in cases where the target posterior can

Table 3.2: Summary of the divide-and-conquer GA employed

**Divide-and-Conquer GA:**

- 8 Local Searches (spatially varying parameters are restricted to the eight compartments, respectively):
  - 250 generations of 80 (160) individuals (Generation 0 is randomly initialized);
  - 1 elite individual is retained for next generation;
  - $k = 8$ -tournament selection selects 80 (160) parents for crossover
  - 80 (160) parents undergo single-point crossover with a success rate of 85%
  - 79 (159) children (one child is discarded) undergo Gaussian mutation with a success rate of 0.75%.
- 1 Global Search (spatially varying parameters are unrestricted):
  - 250 generations of 80 (160) individuals (Generation 0 is composed of best individuals from eight local searches);
  - 1 elite individual is retained for next generation;
  - $k = 8$ -tournament selection selects 80 (160) parents for crossover
  - 80 (160) parents undergo single-point crossover with a success rate of 85%
  - 79 (159) children (one child is discarded) undergo Gaussian mutation with a success rate of 0.75%.

have multiple modes, very large mixing times might be required which may sometimes render the method impractical or infeasible. Furthermore, in MCMC techniques, it can be difficult to design a good proposal distribution when operating in high dimensional spaces. These problems are amplified if the posterior distribution is multi-modal (*i.e.* several significantly different scenarios are likely, given the available data).

In this paper, we propose the use of *Sequential Monte Carlo* (SMC) techniques.

These techniques represent a set of flexible, parallelizable, simulation-based methods for sampling from a sequence of probability distributions [71, 28, 60] (as with MCMC methods, the target distribution(s) need only be known up to a constant). SMC techniques utilize a set of random samples (commonly referred to as *particles*), which are propagated using a combination of *importance sampling*, *resampling*, and MCMC-based *rejuvenation* mechanisms [26, 25]. Each of these particles corresponds to a different value of the model parameters and is associated with an *importance weight* which is proportional to the the posterior value of the respective particle. These weights are updated sequentially along with the particle locations. Hence, if  $\{\Theta^{(m)}, w^{(m)}\}_{m=1}^M$  represent  $M$  such particles and associated weights for the distribution  $\pi(\Theta)$ , then:

$$\pi(\Theta) \approx \sum_{m=1}^M W^{(m)} \delta_{\Theta^{(m)}}(\Theta) \quad (3.17)$$

where  $W^{(m)} = w^{(m)} / \sum_{m=1}^M w^{(m)}$  are the normalized weights and  $\delta_{\Theta^{(m)}}(\cdot)$  is the Dirac function centered at  $\Theta^{(m)}$ . Furthermore, for any function,  $h(\Theta)$ , which is  $\pi$ -integrable, Equation (3.17) almost surely behaves as [24]:

$$\sum_{m=1}^M W^{(m)} h(\Theta^{(m)}) \rightarrow \int h(\Theta) \pi(\Theta) d\Theta \quad (3.18)$$

In order to facilitate sampling, we define a sequence of densities,  $\pi_\gamma$ , indexed by the parameter  $\gamma \in [0, 1]$  as follows:

$$\pi_\gamma(\Theta) = L^\gamma(\Theta) p(\Theta) \quad (3.19)$$

where  $\gamma$  plays the role of *reciprocal temperature* in simulated annealing [83]. Trivially, for  $\gamma = 0$  we recover the prior  $p(\Theta)$  and for  $\gamma = 1$ , the posterior (*i.e.* Equation (3.6)). For small  $\gamma$ , the impact of the data is subdued and  $\pi_\gamma$  can be easily sampled as it is close to the tractable prior. As  $\gamma$  increases,  $\pi_\gamma$  approaches the

target posterior. The role of these auxiliary distributions is therefore to bridge the gap between the prior and posterior and provide a smooth transition path where importance sampling can be efficiently applied. Starting with a particulate approximation of  $\pi_{\gamma=0}$  (which trivially involves drawing samples from the prior with weights  $w^{(m)} = 1$ ), the goal is to gradually update the importance weights and particle locations in order to approximate the intermediate bridging distributions. Naturally, as the number of intermediate distributions increases, the transition path becomes smoother. At the same time however, the computational cost is larger, since sampling from any of these distributions implies likelihood evaluations and therefore calls to the (generally expensive) forward solver. We have developed an adaptive SMC scheme (summarized in Table 3.3 and explained in detail in [60]) where the necessary number of intermediate distributions is determined automatically so as to retain a prescribed level of accuracy in the particulate approximations.

### 3.4 Results and Discussion

Results from the two example problems discussed in the Sections 3.3.1 and 3.3.2 are now presented. Two test cases for each of these example problems are examined using the solution techniques outlined in Sections 3.3.3 and 3.3.3. As a means of quantifying the success of the two approaches as well as the consistency of the solution between the GA runs, the following metric is used:

$$e = \frac{\|\mathbf{\Gamma}_{\text{tar}} - \mathbf{\Gamma}_{\text{sol}}\|_{\ell^2}}{\|\mathbf{\Gamma}_{\text{tar}}\|_{\ell^2}} \quad (3.20)$$

where  $\mathbf{\Gamma}_{\text{tar}}$  represents a collection of the target section properties employed to simulate the observed response,  $\mathbf{U}_{\text{obs}}$ , while  $\mathbf{\Gamma}_{\text{sol}}$  represents a collection of section

Table 3.3: Basic steps of the *Adaptive* SMC algorithm employed

**Adaptive SMC algorithm:**

1. Let  $\gamma_j$ ,  $j = 0, 1, 2, \dots$  be an increasing sequence of  $\gamma$ 's such that  $\gamma_0 = 0$
2. For  $j = 0$ , let  $\{\Theta_0^{(m)}, w_0^{(m)}\}_{m=1}^N$  be the initial particulate approximation to  $\pi_{\gamma_0}$  and  $ESS_0$  the associated effective sample size [28]. Set  $j = 1$ .
3. *Reweigh*: If  $w_j^{(m)}(\gamma_j) = w_{j-1}^{(m)} \frac{\pi_{\gamma_j}(\Theta_{j-1}^{(m)})}{\pi_{\gamma_{j-1}}(\Theta_{j-1}^{(m)})}$  are the *updated* weights as a function of  $\gamma_j$  then determine  $\gamma_j$  so that the associated  $ESS_j = \zeta ESS_{j-1}$  (the value  $\zeta = 0.95$  was used in all the examples). Calculate  $w_j^{(m)}$  for this  $\gamma_j$ .
4. *Resample*: If  $ESS_j \leq ESS_{min}$  then resample (the value  $ESS_{min} = M/2$  was used in all the examples).
5. *Rejuvenate*: Use an MCMC kernel  $P_j(.,.)$  that leaves  $\pi_{\gamma_j}$  invariant to perturb each particle  $\Theta_{j-1}^{(m)} \rightarrow \Theta_j^{(m)}$
6. The current population  $\{\Theta_j^{(m)}, w_j^{(m)}\}_{m=1}^N$  provides a particulate approximation of  $\pi_{\gamma_s}$  in the sense of Equations (3.17), (3.18).
7. If  $\gamma_j < 1$  then set  $j = j + 1$  and goto to step 3. Otherwise stop.

properties emanating from the GA solution (*i.e.* the “optimal” solution) or the SMC solution, which in all cases was based on a population of  $M = 500$  particles. The following values were used for the hyperparameters of the prior model in Section 3.2.3, given by Equation (3.16):

- $k_{max} = 100$  and  $s = 0.1$
- $a_\tau = 1.0$  and  $a_\mu = 0.0001$
- $a_0 = 2.0$  and  $b_0 = 1 \times 10^{-6}$
- $a = 2.0$  and  $b = 1 \times 10^{-6}$  (Equation (3.15))

### 3.4.1 Example Problem 1

Details of the two test cases examined for Example Problem 1 are given in Table 3.4, where values under the heading “Location” represent the center(s) of the damage, and negative numbers under the subsequent  $\hat{j}$  - *Coord.* sub-heading indicate the port side of the ship. The first test case, “Test Case A,” provides a rather straightforward problem, in that a single, large corrosion pattern is the target damage scenario. Conversely, in the second test case, “Test Case B,” the ability of the divide-and-conquer solution scheme to accommodate optimal solutions from *different* local solution spaces is examined. Illustrations of these target damage scenarios are given in Figures 3.8a and 3.11a.

Table 3.4: Test cases examined for Example Problem 1

Test Case	Location (in)		Size (in)		Severity (in)
	$\hat{i}$ -Coord.	$\hat{j}$ -Coord.	$\hat{i}$ -Dir.	$\hat{j}$ -Dir.	
A	3270	-260	240	240	4
B	4445	-260	240	120	4
	2095	260	240	120	4

With respect to Test Case A, an examination of Figure 3.8 reveals that the GA solution (Figure 3.8b) clearly predicts damage in the correct location, with the shape being slightly “thinner,” longitudinally, than the shape of the target damage scenario (Figure 3.8a). It is possible that the upper bound on the number of RBFs (arbitrarily set at  $N_{\max} = 4$ ) may be to blame for this a result, given that all five of the GA runs produced similar results *and* employed the maximum number of RBFs. However, while an increase of this upper bound would allow for a better approximation, the resulting time required to converge to a solution can increase dramatically, given that the number of parameters goes as  $4 \times N$ .

The Bayesian formulation to the problem also leads to accurate identification of the damage scenario as seen in Figure 3.8c. However, an advantage of the proposed framework is that apart from single-point estimates as in Figure 3.8c, the analysis can lead to quantification of the uncertainty due to noise in the data. In Figure 3.9, for example, posterior statistics with regard to the thickness variation are depicted. Furthermore, in Figure 3.10 the posterior density on the standard deviation of the noise in the data is shown which is in good agreement with the reference value. Finally, the metric values computed for each of the GA runs and by averaging over the 500 particles generated in the SMC runs, given in Table 3.5, provide evidence of the consistency between each run.

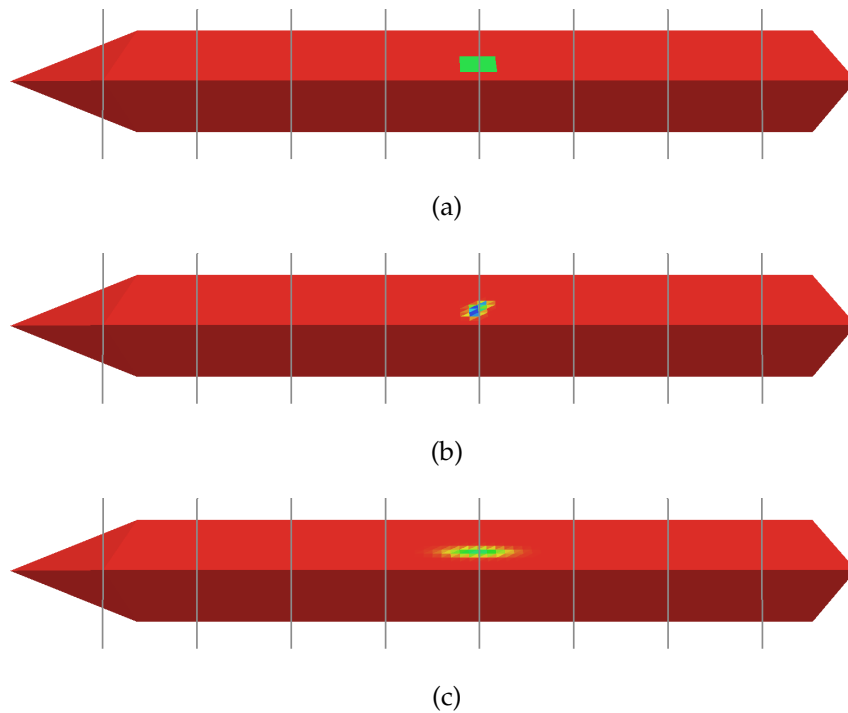
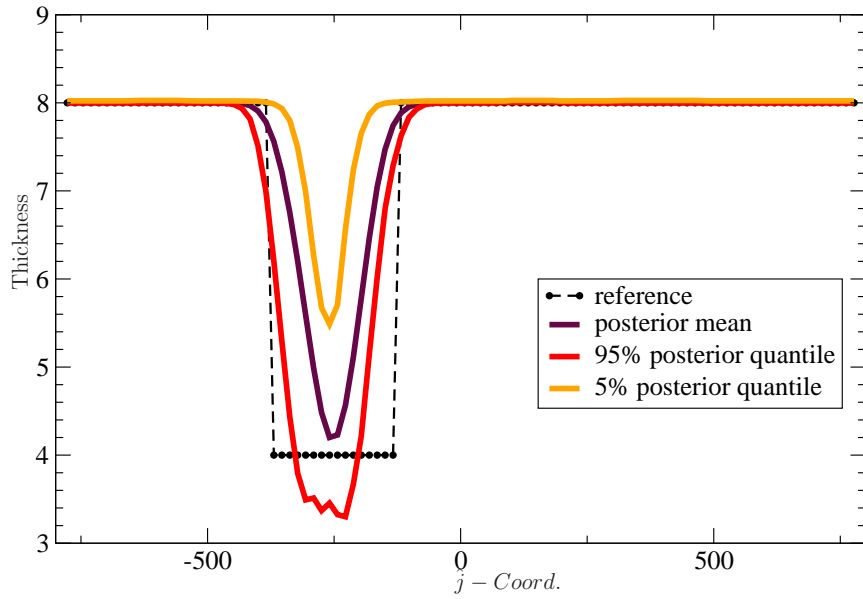
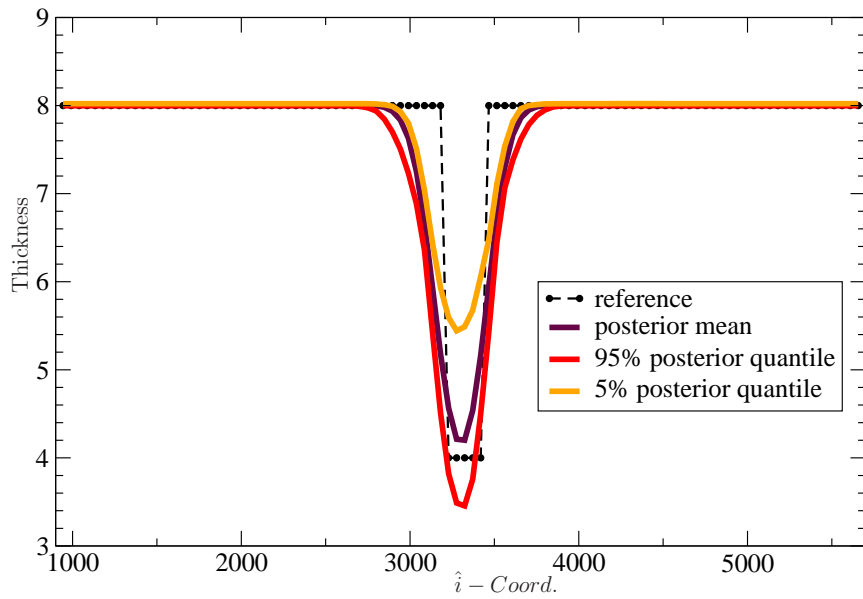


Figure 3.8: Example Problem 1 - Test Case A (a) target damage configuration; (b) representative solution from the GA; (c) maximum likelihood solution from the SMC (gray lines indicate locations of transverse bulkheads)

Considering now Test Case B, a similar examination of Figure 3.11 illustrates the consistency between the GA solution (Figure 3.11b) and the target damage



(a)



(b)

Figure 3.9: Example Problem 1, Test Case A - Posterior mean and posterior quantiles of thickness variation along lines at (a)  $\hat{i} - Coord. = 3270$  and (b)  $\hat{j} - Coord. = -260$  obtained using the Bayesian inference scheme described in Section 3.3.3

scenario (Figure 3.11a). As in Test Case A, the shape is at issue, and it is likely that the above explanation applies to this test case as well. However, the results

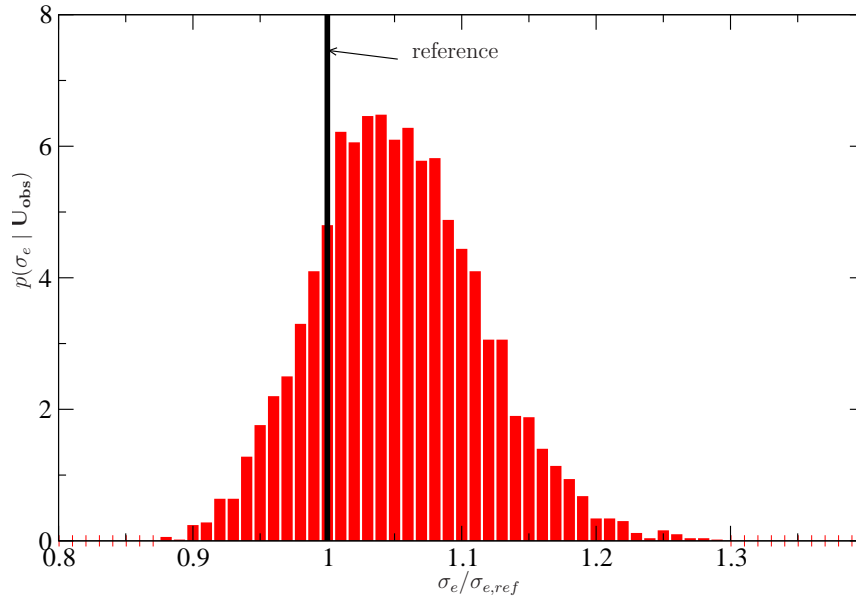


Figure 3.10: Example Problem 1, Test Case A - Posterior density of error standard deviation  $\sigma_e$  (Equation (3.13)) compared with the reference value  $\sigma_{e,ref} = 0.033$  used in generating the data  $U_{obs}$

from this test case reveal a significant conclusion: the divide-and-conquer solution scheme *can* accommodate optimal solutions from *different* local solution spaces. Indeed, an examination of early generations from the final GA execution, searching over the global solution space, revealed that a single corrosion pattern was the optimal solution. However, after these early generations were complete, the second corrosion pattern became part of the updated optimal solution. This result almost certainly emanates from the two disparate solutions exchanging their respective optimal traits through the crossover function. Figures 3.12 and 3.13 depict the estimated posterior statistics for the thickness variation and noise's standard deviation, respectively. Again, it is evident from Table 3.5 that the solutions are consistent for all five of the GA runs and the SMC run.

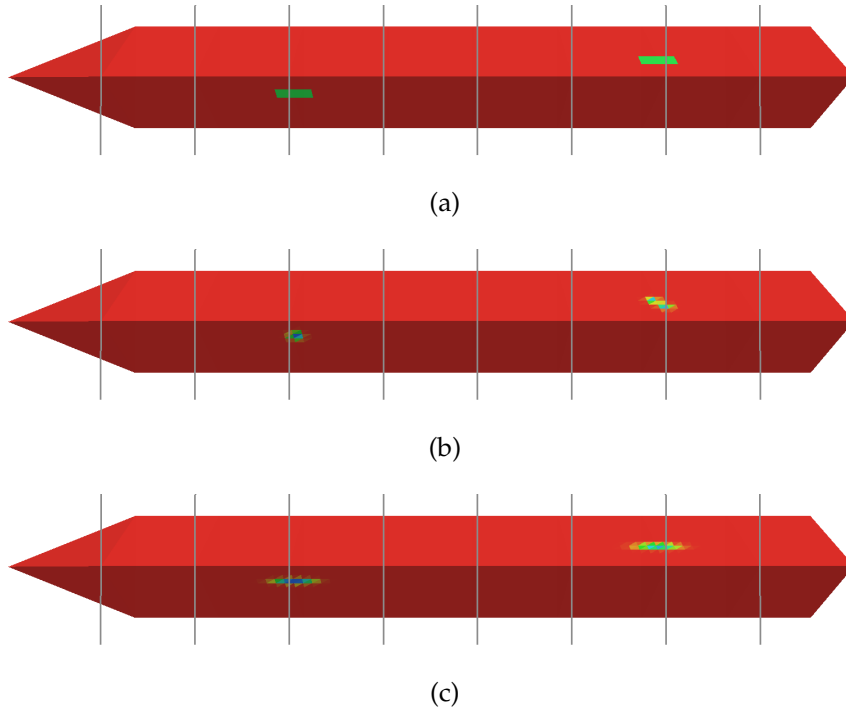


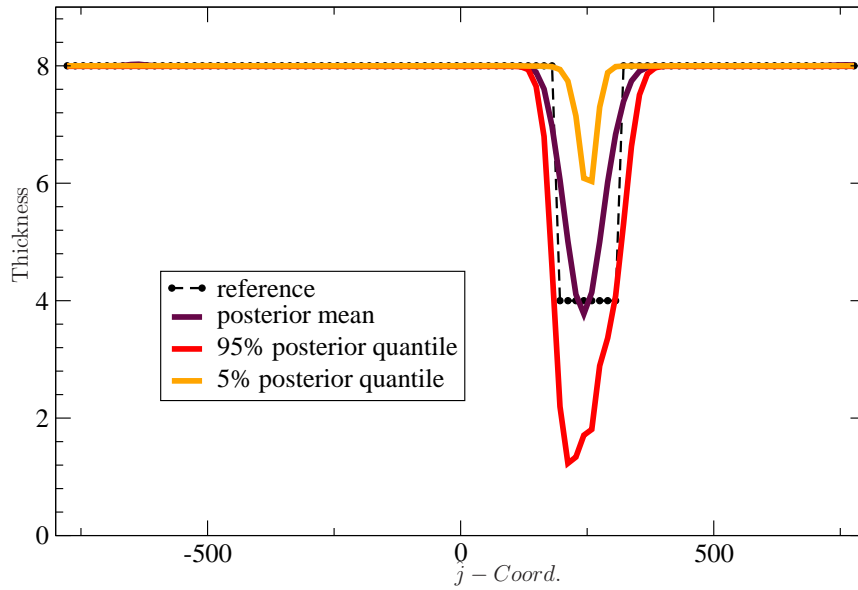
Figure 3.11: Example Problem 1 - Test Case B (a) target damage configuration; (b) representative solution from the GA; (c) maximum likelihood solution from the SMC (gray lines indicate locations of transverse bulkheads)

Table 3.5: Comparison metric values (Equation (3.20)) for Example Problem 1. In the SMC columns the average  $\pm$  st. deviation values are provided which were estimated from the particles approximating the posterior.

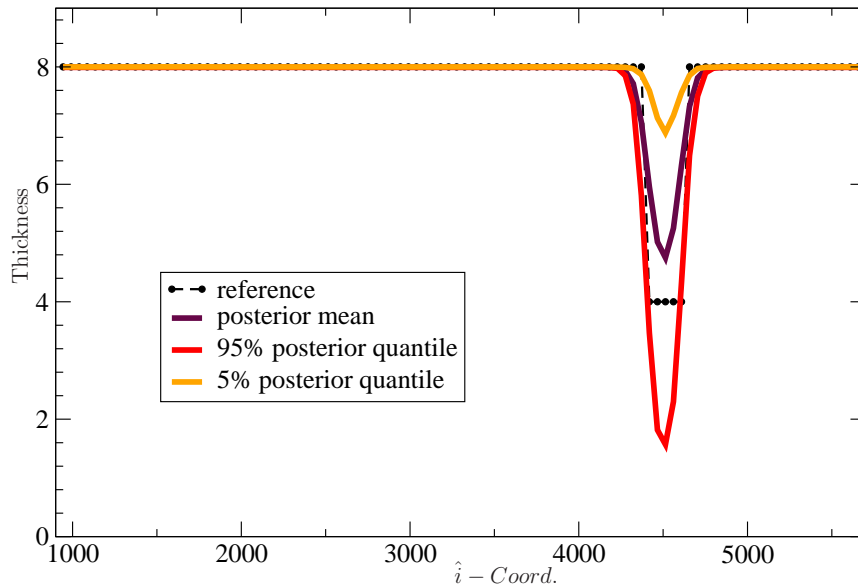
	Test Case A		Test Case B	
Run	GA	SMC	GA	SMC
1	1.143e-3	0.904e-3 $\pm$ 0.185e-3	1.231e-3	0.998e-3 $\pm$ 0.366e-3
2	1.196e-3		1.412e-3	
3	1.221e-3		1.391e-3	
4	1.086e-3		1.316e-3	
5	1.012e-3		1.249e-3	

### 3.4.2 Example Problem 2

Shifting attention to Example Problem 2, Table 3.4 presents the details of the target damage scenarios examined in each of the two test cases. The shapes



(a)



(b)

Figure 3.12: Example Problem 1, Test Case B - Posterior mean and posterior quantiles of thickness variation along lines at (a)  $\hat{i} - Coord. = 2095$  and (b)  $\hat{j} - Coord. = 260$  obtained using the Bayesian inference scheme described in Section 3.3.3

represented by these test cases are more like a “bullseye” than the rectangular shapes examined in the previous example problem. This choice emanates from

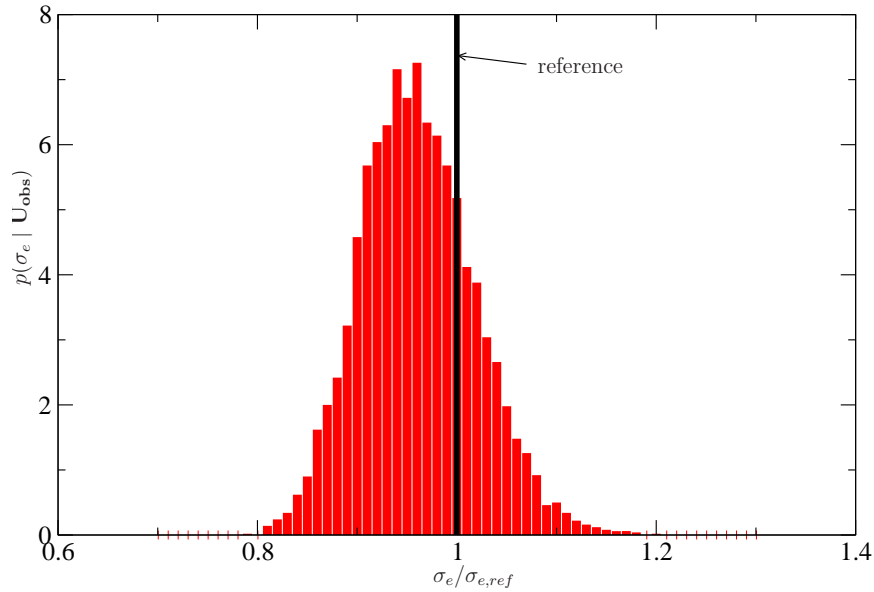


Figure 3.13: Example Problem 1, Test Case B - Posterior density of error standard deviation  $\sigma_e$  (Equation (3.13)) compared with the reference value  $\sigma_{e,ref} = 0.033$  used in generating the data  $\mathbf{U}_{obs}$

the fact that framing damage due to an internal explosion forms the focus of this example problem. As in Example Problem 1, Test Case A provides a more straightforward problem, whereas Test Case B provides somewhat more of a challenge to the GA. However, in order to further examine the capabilities of the divide-and-conquer strategy, Test Case A actually represents two internal explosions which end up being linked through the less severely damaged regions surrounding their respective centers. The question here relates to whether two blasts from *coincident* compartments can be detected separately versus being lumped together as a single explosion representation. Illustrations of these target damage scenarios are given in Figures 3.14a and 3.15a.

The answer to the above question is quickly answered upon inspection of results given in Figure 3.14. Indeed, solutions from all of the GA runs reproduced the dual explosion as a single explosion. This result, however, is not terribly sur-

Table 3.6: Test cases examined for Example Problem 2

Test Case	Location (in)		Severity (in)
	$\hat{i}$ -Coord.	$\hat{j}$ -Coord.	
A	3420	-372	8
	3180	-248	8
B	1740	-372	10
	5280	-372	6
	5400	-248	6

prising when considering the close proximity of the two explosions in addition to the fact that they occur in different compartments. Recalling the restrictions on the spatial parameters during local GA executions, it is seen that while a single blast occurs in each of two coincident compartments, a more viable solution may instead straddle the compartments, thus capturing the *overall* effects of the target damage scenario through a single explosion representation. In this case, therefore, the divide-and-conquer strategy may actually have done more harm than good. Nevertheless, damage predicted by the GA is clearly located in the proximity of the target location, with the results between each of the GA runs exhibiting consistency as given by the computed metric values given in Table 3.7.

With respect to Test Case B, an examination of Figure 3.15 reveals some of the same characteristics of the divide-and-conquer strategy as seen in previous three test cases. First, the capability of the solution strategy to combine optimal solutions from different local solution spaces is clearly demonstrated. However, with respect to the explosion pattern at the aft end of the ship, it is again seen that the *overall* effect of the damage is captured, but the shape of the GA solution (Figure 3.15b) differs from that of the target damage scenario (Figure 3.15a).

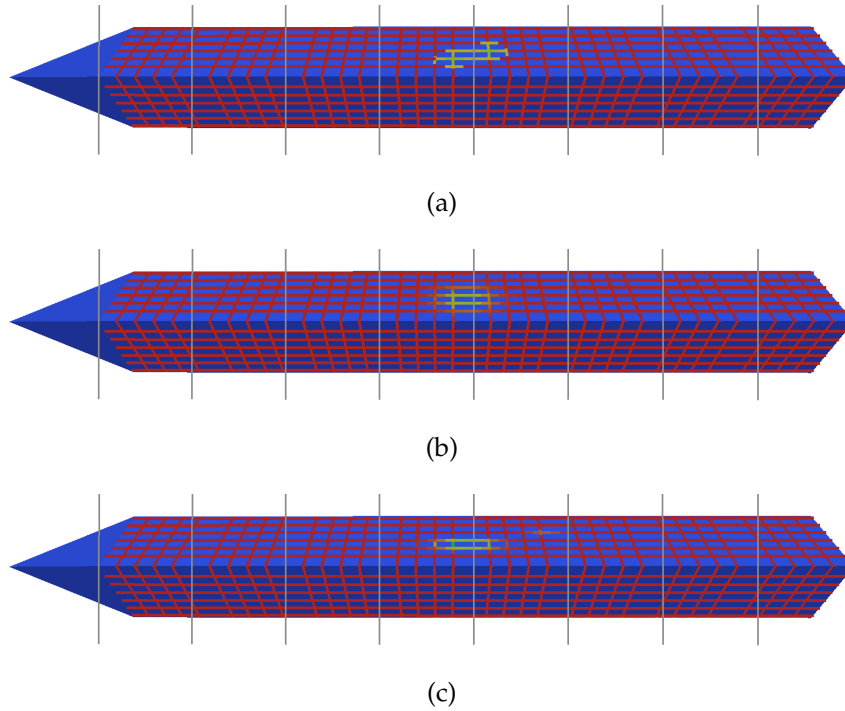


Figure 3.14: Example Problem 2 - Test Case A (a) target damage configuration; (b) representative solution from the GA; (c) maximum likelihood solution from the SMC (gray lines indicate locations of transverse bulkheads)

Again, this is likely due to the upper bound on the number of RBFs (also arbitrarily set at  $N_{\max} = 4$ ). Finally, the metric values for this test case are given in Table 3.7, with the first four GA runs producing relatively consistent solutions, and the fifth GA run producing a poor result. Upon further examination of this run, it appears that the solution simply did not converge prior to the maximum number of generations. While convergence of the solution did not appear to be an issue during any of the other 19 runs executed for this paper, a more robust stopping criteria is worth consideration for future research efforts.

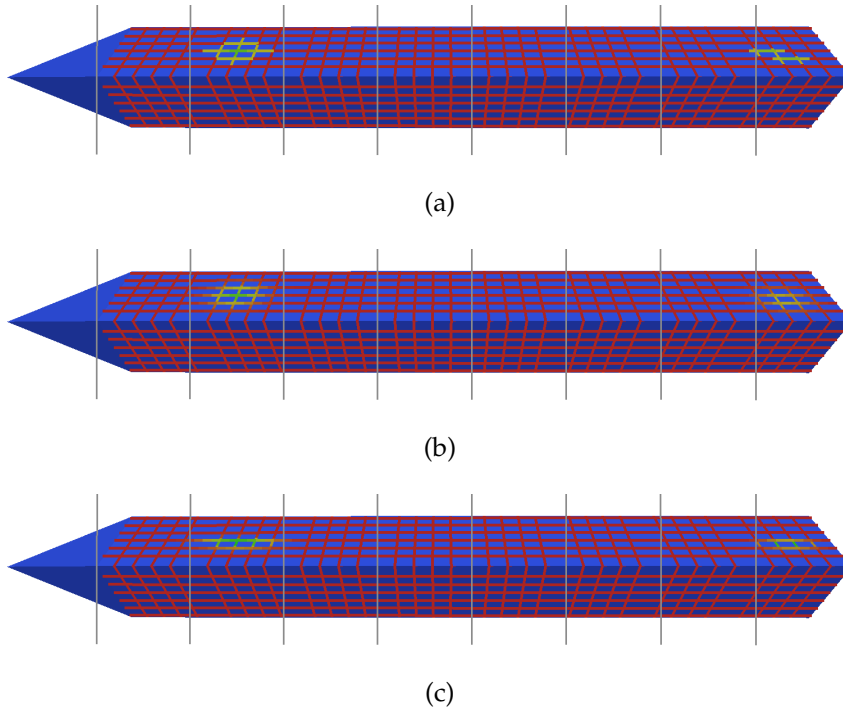


Figure 3.15: Example Problem 2 - Test Case B (a) target damage configuration; (b) representative solution from the GA; (c) maximum likelihood solution from the SMC (gray lines indicate locations of transverse bulkheads)

Table 3.7: Comparison metric values (Equation (3.20)) for Example Problem 2. In the SMC columns the average  $\pm$  st. deviation values are provided which were estimated from the particles approximating the posterior.

Run	Test Case A		Test Case B	
	GA	SMC	GA	SMC
1	7.366e-4	7.966e-4 $\pm$ 12.269e-4	4.400e-4	58.057e-4 $\pm$ 33.196e-4
2	5.254e-4		7.194e-4	
3	4.885e-4		6.731e-4	
4	5.518e-4		4.687e-4	
5	5.637e-4		24.535e-4	

### 3.5 Conclusions

The ever-changing conditions within which the naval fleets operate provide a strong motivation for the need to treat health monitoring within the context of

full-scale ship structural systems. The present paper aimed to treat the HSHM problem within a model-based context, *vis-à-vis* two approaches: a classical or optimization-based approach adopting a divide-and-conquer genetic algorithm and a Bayesian statistical inference approach adopting a sequential Monte Carlo algorithm.

The results presented herein demonstrate the promise of applying the model-based approach to HSHM in full-scale ship structural systems. The classical approach consistently produced reasonable point estimates of the target solutions, making it a viable choice for this application. However, given the uncertainty typically associated with the operating conditions of ocean-going vessels, it is the authors' opinions that the Bayesian approach to the problem demonstrates the most promise for future research efforts. The direct, quantitative treatment of uncertainty within the inferred damage predictions, as provided by the Bayesian solution schemes, provides the framework necessary to begin examining the final step in the SHM paradigm: damage prognosis.

## **Acknowledgments**

The authors gratefully acknowledge the Office of Naval Research, Division 331, Ship System and Engineering Research, for their support of this work through Grants N00014-07-1-0515 and N00014-09-1-0310. The authors would also like to thank Dr. Paul Hess of Division 331 for his many helpful discussions.

## BIBLIOGRAPHY

- [1] Federal Highway Administration. Count of bridges by structure type, November 2007. <http://www.fhwa.dot.gov/bridge/strtyp06.htm>.
- [2] KE. Andersen, SP. Brooks, and M. B. Hansen. Bayesian inversion of geoelectrical resistivity data. Technical report, Dept. Math. Sci., Aalborg University, 2001.
- [3] J. Arbocz. The imperfection data bank, a means to obtain realistic buckling loads. In Proceedings of the Buckling of Shells - A State-of-the-art colloquium, Springer, Berlin, 1982.
- [4] K.J. Bathe. Finite Element Procedures. Prentice-Hall, Inc., Englewood Cliffs, New Jersey, 1st edition, 1996.
- [5] K.J. Bathe and E.N. Dvorkin. On the automatic solution of nonlinear finite element equations. Computers and Structures, 17(5-6):871-879, 1983.
- [6] K.J. Bathe and E.N. Dvorkin. A four-node plate bending element based on mindlin / reissner plate theory and a mixed interpolation. International Journal for Numerical Methods in Engineering, 21:367-383, 1985.
- [7] K.J. Bathe and E.N. Dvorkin. A formulation of general shell elements - the use of mixed interpolation of tensorial components. International Journal for Numerical Methods in Engineering, 22:697-722, 1986.
- [8] K.J. Bathe and L.W. Ho. A simple and effective element for analysis of general shell structures. Computers and Structures, 13(5-6):673-81, 1981.
- [9] J.L. Batoz. An explicit formulation for an efficient triangular plate-bending element. International Journal for Numerical Methods in Engineering, 18(7):1077-89, 1982.
- [10] J.L. Batoz, K.J. Bathe, and L.W. Ho. A study of three-node triangular plate bending elements. International Journal for Numerical Methods in Engineering, 15(12):1771-812, 1980.
- [11] Z.P. Bazant and L. Cedolin. Stability of Structures. Oxford university Press, 1991.

- [12] T. Belytschko, W.K. Liu, and B. Moran. Nonlinear Finite Elements for Continua and Structures. John Wiley and Sons, Inc., 2000.
- [13] E. Bielewicz and J. Gorski. Shells with random geometric imperfections, simulation-based approach. International Journal of Non-Linear Mechanics, 37:777–784, 2002.
- [14] A. Budipriyanto, M.R. Haddara, and A.S.J. Swamidas. Crack identification in a cross-stiffened plate system using the root mean square of time domain responses. Canadian Journal of Civil Engineering, 33(8):989–1004, 2006.
- [15] A. Budipriyanto, A.S.J. Swamidas, and M.R. Haddara. Identification of small-sized cracks on cross-stiffened plate structures for ships. Journal of Engineering Materials and Technology, 128(2):210–24, 2006.
- [16] R.L. Burden and J.D. Faires. Numerical Analysis. Thomson Brooks / Cole, Belmont, California, 8th edition, 2005.
- [17] J. Ching, J.L. Beck, K.A. Porter, and R. Shaikhutdinov. Bayesian state estimation method for nonlinear systems and its application to recorded seismic response. Journal of Engineering Mechanics, 132(4):396–410, 2006.
- [18] T. Colton. U.S Shipbuilding History, April 2009. <http://shipbuildinghistory.com/>.
- [19] SolidWorks Corporation. Solidworks office, 2006. Version 2007 (SP1.1).
- [20] PS Craig, M Goldstein, JC Rougier, and AH Seheult. Bayesian forecasting for complex systems using computer simulators. JOURNAL OF THE AMERICAN STATISTICAL ASSOCIATION, 96(454):717 – 729, 2001.
- [21] M.A. Crisfield. On an approximate yield criterion for thin shells. Technical Report LR658, Transport and Road Research Laboratory, Crowthorne, Berkshire, 1974.
- [22] M.A. Crisfield. Ivanov’s yield criterion for thin steel plates and shells using finite elements. Technical Report LR919, Transport and Road Research Laboratory, Crowthorne, Berkshire, 1979.
- [23] C. Darwin. The Origin of Species. Bantam Books, 1859.

- [24] P. Del Moral. Feynman-Kac Formulae: Genealogical and Interacting Particle Systems with Applications. Springer New York, 2004.
- [25] P. Del Moral, A. Doucet, and A. Jasra. Sequential monte carlo for bayesian computation (with discussion). In Bayesian Statistics 8. Oxford University Press, 2006.
- [26] P. Del Moral, A. Doucet, and A. Jasrau. Sequential Monte Carlo Samplers. Journal of the Royal Statistical Society B, 68(3):411–436, 2006.
- [27] L.H. Donnell. Beams, Plates and Shells. McGraw-Hill, 1976.
- [28] A. Doucet, J. F. G. de Freitas, and N. J. Gordon, editors. Sequential Monte Carlo Methods in Practice. Springer New York, 2001.
- [29] E.N. Dvorkin and K.J. Bathe. A continuum mechanics based four-node shell element for general nonlinear analysis. Engineering Computations, 1:77–88, 1983.
- [30] C.J. Earls. Observations on eigenvalue buckling analysis within a finite element context. In Proceedings of the Structural Stability Research Council, Annual Stability Conference, New Orleans, LA, USA, 2007.
- [31] B.L.O. Edlund. Buckling of metallic shells: Buckling and postbuckling behaviour of isotropic shells, especially cylinders. Structural Control and Health Monitoring, 14:693–713, 2007.
- [32] A.A. El Damatty and A.O. Nassef. A finite element optimization technique to determine critical imperfections of shell structures. Structural and Multidisciplinary Optimization, 23:75–87, 2001.
- [33] S. El-Tawil, E. Severino, and P. Fonseca. Vehicle collision with bridge piers. Journal of Bridge Engineering, 10(3):345–53, 2005.
- [34] C.R. Farrar, S.W. Doebling, and D.A. Nix. Vibration-based structural damage identification. Philosophical Transactions of The Royal Society A, 359(1778):131–49, 2001.
- [35] C.R. Farrar, G. Park, M. Angel, M.T. Bement, and L. Salvino. Structural health monitoring for ship structures. In Proceedings of the 7th International Workshop on Structural Health Monitoring 2009: From

Systems Integration to Autonomous Systems, pages 1970–7, Stanford, California, September 2009.

- [36] C.R. Farrar and K. Worden. An introduction to structural health monitoring. Philosophical Transactions of The Royal Society A, 365(1851):303–15, 2007.
- [37] C.A. Featherston. Imperfection sensitivity of curved panels under combined compression and shear. International Journal of Non-Linear Mechanics, 38:225–238, 2003.
- [38] M. Ferreira and H. Lee. Multiscale Modeling - A Bayesian Perspective. Springer Series in Statistics. Springer, 2007.
- [39] M.I. Friswell. Damage identification using inverse methods. Philosophical Transactions of The Royal Society A, 365(1851):393–410, 2007.
- [40] C.C. Fu, J.R. Burhouse, and G.L. Chang. Overheight vehicle collisions with highway bridges. Journal of the Transportation Research Board, 1865:80–8, 2004.
- [41] P.A. Fuchs, G.A. Washer, S.B. Chase, and M. Moore. Applications of laser-based instrumentation for highway bridges. Journal of Bridge Engineering, 9(6):541–9, 2004.
- [42] P.A. Fuchs, G.A. Washer, S.B. Chase, and M. Moore. Laser-based instrumentation for bridge load testing. Journal of Performance of Constructed Facilities, 18(4):213–9, 2004.
- [43] R.H. Gallagher, R.A. Gellatly, J. Padlog, and R.H. Mallett. A discrete element procedure for thin-shell instability analysis. AIAA Journal, 5(1):138–145, 1967.
- [44] RE Glaser, G. Johannesson, S Sengupta, B Kosovic, and S Carle. Stochastic engine final report: Applying markov chain monte carlo methods with importance sampling to large-scale data-driven simulation. Technical report, Lawrence Livermore National Lab., Livermore, CA, 2004.
- [45] J. Goedert, J. Bonsell, and F. Samura. Integrating laser scanning and rapid prototyping to enhance construction modeling. Journal of Architectural Engineering, 11(2):71–4, 2004.

- [46] D.E. Goldberg. Genetic Algorithms in Search, Optimization, and Machine Learning. Addison-Wesley Publishing Co., Inc., Reading, Massachusetts, 1st edition, 1989.
- [47] S.J. Gould. The Structure of Evolutionary Theory. Harvard University Press, 2002.
- [48] R.L. Hardy. Theory and applications of the multiquadric-biharmonic method. Computers & Mathematics with Applications, 19(8-9):163–208, 1990.
- [49] R.L. Haupt and S.E. Haupt. Practical Genetic Algorithms. John Wiley and Sons, Inc., New York, New York, 2nd edition, 2004.
- [50] BK Hegstad and H Omre. Uncertainty in production forecasts based on well observations, seismic data, and production history. SPE JOURNAL, 6(4):409 – 424, 2001.
- [51] I. Herszberg, H.C.H. Li, F. Dharmawan, A.P. Mouritz, M. Nguyen, and J. Bayandor. Damage assessment and monitoring of composite ship joints. Composite Structures, 67(2):205–216, 2005.
- [52] D Higdon, H Lee, and ZX Bi. A bayesian approach to characterizing uncertainty in inverse problems using coarse and fine-scale information. IEEE TRANSACTIONS ON SIGNAL PROCESSING, 50(2):389 – 399, 2002.
- [53] S.M. Holzer, J.F. Davalos, and C.Y. Huang. A review of finite element stability investigations of spatial wood structures. Bulletin of the International Association for Shell and Spatial Structures, 31(2):161–171, 1990.
- [54] M. Hubler and C.J. Earls. Comparison of finite element based eigenvalue buckling approaches. Steel and Composite Structures, pages ?–?, 2008 - In Review.
- [55] G.W. Hunt, G.J. Lord, and M.A. Peletier. Cylindrical shell buckling: A characterization of localization and periodicity. Discrete and Continuous Systems - Series B, 3(4):505–518, 2003.
- [56] ADINA Research & Development Inc. Adina, 2006. Version 8.4.1.
- [57] Autodesk Inc. Autocad, 2005. Version 2006.

- [58] Geomagic Inc. Geomagic studio, 2006. Version 9 (SR 2).
- [59] PK Kitanidis. Parameter uncertainty in estimation of spatial functions - bayesian-analysis. WATER RESOURCES RESEARCH, 22(4):499 – 507, 1986.
- [60] P.S. Koutsourelakis. A multi-resolution, non-parametric, Bayesian framework for identification of spatially-varying model parameters. Journal of Computational Physics, 228(17):6184–6211, 2009.
- [61] E. Kreyszig. Introductory Functional Analysis with Applications. John Wiley and Sons, Inc., 1978.
- [62] H.P. Langtangen. Computational Partial Differential Equations. Springer, 2000.
- [63] H. Lee, D. Higdon, Z. Bi, M. Ferreira, and M. West. Markov random field models for high-dimensional parameters in simulations of fluid flow in porous media. TECHNOMETRICS, 44(3):230 – 241, 2002.
- [64] H.C.H. Li, I. Herszberg, C.E. Davis, A.P. Mouritz, and S.C. Galea. Health monitoring of marine composite structural joints using fibre optic sensors. Composite Structures, 75(1–4):321–7, 2006.
- [65] D.D. Lichti, S.J. Gordon, and T. Tipdecho. Error models and propagation in directly georeferenced terrestrial laser scanner networks. Journal of Surveying Engineering, 131(4):135–42, 2005.
- [66] K. Lindemann, J. Odland, and J. Strengehagen. On the application of hull surveillance systems for increased safety and improved structural utilization in rough weather. Technical Report 105-Febr, Det Norske Veritas, Hovik, Norway, 1978.
- [67] F Liu, MJ Bayarri, JO Berger, R Paulo, and J Sacks. A bayesian analysis of the thermal challenge problem. COMPUTER METHODS IN APPLIED MECHANICS AND ENGINEERING, 197(29-32):2457 – 2466, 2008.
- [68] G.R. Liu and X. Han. Computational Inverse Techniques in Nondestructive Evaluation. CRC Press LLC, Boca Raton, Florida, 1st edition, 2003.

- [69] J.S. Liu. Monte Carlo Strategies in Scientific Computing. Springer Series in Statistics. Springer, 2001.
- [70] J.P. Lynch, R.A. Swartz, A.T. Zimmerman, T.F. Brady, J. Rosario, L.W. Salvino, and K.H. Law. Monitoring of a high speed naval vessel using a wireless hull monitoring system. In Proceedings of the 7th International Workshop on Structural Health Monitoring 2009: From Systems Integration to Autonomous Systems, pages 1926–33, Stanford, California, September 2009.
- [71] S.N. MacEachern, M. Clyde, and J.S. Liu. Sequential importance sampling for nonparametric bayes models: The next generation. The Canadian Journal of Statistics / La Revue Canadienne de Statistique, 27(2):251–267, 1998.
- [72] W. McGuire, R.H. Gallagher, and R.D. Ziemian. Matrix Structural Analysis. John Wiley and Sons, Inc., New York, New York, 2nd edition, 2000.
- [73] M. Mitchell. An Introduction to Genetic Algorithms. The MIT Press, Cambridge, Massachusetts, 1st edition, 1998.
- [74] J.M. Nichols, W.A. Link, K.D. Murphy, C.C. Olson, F. Bucholtz, and J.V. Michalowicz. A bayesian approach to identifying and tracking damage in structures. In Proceedings of the 7th International Workshop on Structural Health Monitoring 2009: From Systems Integration to Autonomous Systems, pages 1951–8, Stanford, California, September 2009.
- [75] C.K. Oh, J.L. Beck, and M. Yamada. Bayesian learning using automatic relevance determination prior with an application to earthquake early warning. Journal of Engineering Mechanics, 314(12):1013–20, 2008.
- [76] V. Papadopoulos and M. Papadrakakis. Finite-element analysis of cylindrical panels with random initial imperfections. Journal of Engineering Mechanics, 130(8):867–876, 2004.
- [77] V. Papadopoulos and M. Papadrakakis. The effect of material and thickness variability on the buckling load of shells with random initial imperfections. Computer Methods in Applied Mechanics and Engineering, 194:1405–1426, 2005.
- [78] V. Papadopoulos and I. Pavlos. The effect of non-uniformity of axial

loading on the buckling behavior of shells with random imperfections. International Journal of Solids and Structures, 44:6299–6317, 2007.

- [79] J. Pontow and D. Dinkler. Imperfection sensitivity and limit loads of spherical shells under radial pressure. Proceedings in Applied Mathematics and Mechanics, 5:253–254, 2005.
- [80] J.S. Przemieniecki. Theory of Matrix Structural Analysis. Dover Publications, Inc., 1968.
- [81] A. Ravindran, K.M. Ragsdell, and G.V. Reklaitis. Engineering Optimization: Methods and Applications. John Wiley and Sons, Inc., Hoboken, New Jersey, 2nd edition, 2006.
- [82] B.D. Reddy. Introductory Functional Analysis. Springer, 1998.
- [83] C. P. Robert and G. Casella. Monte Carlo Statistical Methods. Springer New York, 2nd edition, 2004.
- [84] A. Rytter. Vibration based inspection of civil engineering structures. PhD thesis, University of Aalborg, Aalborg, Denmark, 1993.
- [85] K. Sabra and L. Salvino. Using diffuse vibrations interferometry for structural health monitoring of high-speed naval ships. In Proceedings of the 7th International Workshop on Structural Health Monitoring 2009: From Systems Integration to Autonomous Systems, pages 1895–1901, Stanford, California, September 2009.
- [86] C.A. Schenk and G.I. Schuëller. Buckling analysis of cylindrical shells with cutouts including random boundary and geometric imperfections. Computer Methods in Applied Mechanics and Engineering, 196:3424–3434, 2007.
- [87] DM Schmidt, JS George, and CC Wood. Bayesian inference applied to the electromagnetic inverse problem. HUMAN BRAIN MAPPING, 7(3):195 – 212, 1999.
- [88] R.A. Silva-Muñoz and R.A. Lopez-Anido. Structural health monitoring of marine composite structural term joints using embedded fiber bragg grating strain sensors. Composite Structures, 89(2):224–34, 2009.

- [89] J. Singer, J. Arbocz, and T. Weller. Buckling Experiments, Volume 1. John Wiley and Sons, Inc., 1998.
- [90] J. Singer, J. Arbocz, and T. Weller. Buckling Experiments, Volume 2. John Wiley and Sons, Inc., 2002.
- [91] H. Sohn, C.R. Farrar, F.M. Hemez, D.D. Shunk, D.W. Stinemat, and B.R. Nadler. A review of structural health monitoring literature: 1996-2001. Technical Report LA-13976-MS, Los Alamos National Laboratory, Los Alamos, New Mexico, 2003.
- [92] C.J. Stull. On the comparison of computational methods for analyzing longitudinally skewed steel i-girder bridges. Master's thesis, University of Pittsburgh, Pittsburgh, Pennsylvania, 2006.
- [93] C.J. Stull, C.J. Earls, and W. Aquino. A posteriori initial imperfection identification in shell buckling problems. Computer Methods in Applied Mechanics and Engineering, 198(2):260–8, 2008.
- [94] Y.Y. Su, J.N. Oliverira Filho, L.Y. Liu, and Y.M.A. Hashash. Integration of construction field data and geotechnical analyses. In Proceedings of the 2005 Construction Research Congress, Reston, Virginia, April 2005.
- [95] AN. Tikhonov. On the solution of incorrectly put problems and the regularization method. Acad. Sci. USSR Siberian Branch, pages 261–265, 1963.
- [96] M.D. Todd, J.M. Nichols, S.T. Trickey, M. Seaver, C.J. Nichols, and L.N. Virgin. Bragg grating-based fibre optic sensors in structural health monitoring. Philosophical Transactions of The Royal Society A, 365(1851):317–43, 2007.
- [97] H.E. Torkildsen, . Grvlen, A. Skaugen, G. Wang, A.E. Jensen, K. Pran, and G. Sagvolden. Development and applications of full-scale ship hull health monitoring systems for the Royal Norwegian Navy. In Recent Developments in Non-Intrusive Measurement Technology for Military Application on Model- and Full-Scale Vehicles, pages 22–1–22–14, Budapest, Hungary, April 2005. NATO Research and Technology Organisation.
- [98] G. Wang, K. Pran, G. Sagvolden, G.B. Havsgard, A.E. Jensen, G.A. Johnson, and S.T. Vohra. Ship hull structure monitoring using fibre optic sensors. Smart Materials and Structures, 10(3):472–8, 2001.

- [99] JB Wang and N Zabaras. Hierarchical bayesian models for inverse problems in heat conduction. INVERSE PROBLEMS, 21(1):183 – 206, 2005.
- [100] Z. Waszczyszyn and M. Bartczak. Neural prediction of buckling loads of cylindrical shells with geometrical imperfections. International Journal of Non-Linear Mechanics, 37:763–775, 2002.
- [101] IS Weir. Fully bayesian reconstructions from single-photon emission computed tomography data. JOURNAL OF THE AMERICAN STATISTICAL ASSOCIATION, 92(437):49 – 60, 1997.
- [102] K.V. Yuen and J.L. Beck. Reliability-based robust control for uncertain dynamical systems using feedback of incomplete noisy response measurements. Earthquake Engineering and Structural Dynamics, 32(5):751–70, 2003.
- [103] A. Zubaydi, M.R. Haddara, and A.S.J. Swamidas. On the use of the autocorrelation function to identify the damage in the side shell of a ship’s hull. Marine Structures, 13(6):537–51, 2000.
- [104] A. Zubaydi, M.R. Haddara, and A.S.J. Swamidas. Damage identification in a ships structure using neural networks. Ocean Engineering, 29(10):1187–200, 2002.